

# The aqueous geochemistry of the étang de Thau, southern France

Reefe Conley  
Girton College



### **Acknowledgements**

My sincere thanks to Professor Ed Tipper, Professor Sasha Turchyn and Doctor Morag Hunter for their committed supervision and support during this project, and to my fieldwork partners, Gio and Lin, for their enthusiasm and perseverance. Thanks also to my family, and to Liv, for their love and support throughout.

Funding was provided by the Mary Euphrasia Mosley, Sir Bartle Frere's Memorial and Worts Travelling Scholars Funds; Girton College; CASP and the Marr Memorial fund.

## **Abstract**

The étang de Thau, a large lagoon in southern France, shows significant spatial and temporal variation in its aqueous chemistry owing to physical, biological and anthropogenic processes. This project analysed the water chemistry of the étang de Thau and its water inputs using simple chemical tests to identify, quantify and differentiate the effects of these processes. The reliability of this analysis was also considered.

Carbonate weathering and agricultural runoff appear to control the chemistry of the main river feeding the Thau. The chemistry of the lagoon interior appears to be dominated by the Mediterranean Sea. There is evidence that significant evaporation and photosynthesis occurs in the Thau, and that siliceous phytoplankton are present in the lagoon. There is also evidence that intensive shellfish farming and wind-forcing release  $\text{NH}_4^+$  into the Thau water column. Finally, there is evidence of flow reversal and salinisation of a submarine karst aquifer in the lagoon.

## **Notes**

Chemical formulae are used throughout. The concentrations of chemical species are denoted with square brackets.

Map data provided by ©OpenStreetMap under the Open Database License.

## **Word count**

Main text word count (excluding declaration, table of contents, data table, references and figure captions): 5,949.

## **Declaration**

I declare that the submitted work is my own, except where acknowledgement is given to the work of others or to work done in collaboration. I declare that I have read and understood the Department of Earth Sciences statement on plagiarism and that my work could be tested using automated plagiarism software.

Signed:

# Contents

<b>1</b>	<b>Introduction</b>	<b>3</b>
1.1	Project purpose . . . . .	3
1.2	Field area . . . . .	3
1.2.1	The Thau and its catchment . . . . .	3
1.2.2	Geography . . . . .	7
1.2.3	Residence time . . . . .	7
1.3	Initial Hypotheses . . . . .	7
1.4	Logistics . . . . .	8
<b>2</b>	<b>Methods</b>	<b>9</b>
2.1	Data collection and analysis . . . . .	9
2.2	Analyte Rationale . . . . .	9
2.3	Uncertainty . . . . .	9
2.4	Normalised inorganic charge balance . . . . .	10
<b>3</b>	<b>Results</b>	<b>12</b>
3.1	Lithological control on aqueous geochemistry . . . . .	12
3.2	Alkalinity . . . . .	12
3.3	Si . . . . .	12
3.4	$\text{NH}_4^+$ . . . . .	13
3.5	$\text{NO}_3^-$ . . . . .	13
3.6	$\text{PO}_4^{3-}$ . . . . .	13
3.7	Vise salinity . . . . .	13
<b>4</b>	<b>Discussion</b>	<b>22</b>
4.1	Lithological control on aqueous geochemistry . . . . .	22
4.2	Evaporation . . . . .	22
4.3	Photosynthesis . . . . .	24
4.4	Shellfish farming . . . . .	25
4.5	Vise spring structure . . . . .	27
<b>5</b>	<b>Conclusions</b>	<b>28</b>
<b>A</b>	<b>Alkalinity and DIC</b>	<b>29</b>
<b>B</b>	<b>Uncertainty data</b>	<b>30</b>
B.1	Salinity and pH probe uncertainty . . . . .	30
B.2	Titration uncertainty . . . . .	31
B.3	Si uncertainty . . . . .	31
B.4	$\text{PO}_4^{3-}$ uncertainty . . . . .	32
B.5	$\text{NO}_3^-$ -N to $\text{NO}_3^-$ and uncertainty . . . . .	33
B.6	$\text{NH}_3$ -N as a proxy for $\text{NH}_4^+$ and $\text{NH}_3$ -N uncertainty . . . . .	34
<b>C</b>	<b>Data table</b>	<b>36</b>

# 1 Introduction

## 1.1 Project purpose

The purpose of this project was to use simple tests to identify and explain geochemical gradients in any location in the world. The field site selected for this project was the étang de Thau (Thau lagoon), a brackish lagoon on the southeastern coast of France. Owing to its unique geology, geography and environmental setting, the Thau and its watershed show extremely large spatial and temporal gradients in many geochemical analytes. The unique features of the Thau that prompted its use for this project included

1. The low tidal range in the Mediterranean Sea reduces the water exchange between the Thau and outlying marine water, maintaining the lagoon as a semi-enclosed environment. The lagoon was expected to have experienced significant evaporation and show hypersalinity ( $>35$  ppt). This project aimed to identify and quantify the process of evaporation on waters in the Thau.
2. The major river feeding the Thau, along with a submarine spring, are sourced from karst aquifers, so large gradients both in alkalinity and salinity were expected across the mixing zone of river and lagoon waters. Strong gradients in alkalinity and salinity provide a clear background from which to identify non-conservative processes.
3. Intensive shellfish farming occurs year-round in the Thau. The biodeposition associated with this is the primary source of eutrophication (increased total nitrogen and  $\text{PO}_4^{3-}$ ) in the lagoon (De Casabianca, Laugier, and Collart 1997). Eutrophication is associated with high rates of photosynthesis (*Eutrophication* 2024). This project aimed to identify and quantify the effects of photosynthesis and shellfish farming in the lagoon.

To investigate these aspects of the field site, the project aimed to distinguish between conservative mixing between waters of different chemical identities along with any non-conservative processes that may be occurring in the lagoon. Water masses mix conservatively with respect to a constituent when it is neither added nor removed from the mixing system, and hence the constituent shows a linear relationship when plotted against a conservative tracer, such as total salinity. Non-conservative processes, such as photosynthesis, alter the concentrations of the constituents of water. When the concentration of a constituent of water is plotted against a conservative tracer, non-conservative processes can be identified as deviations from linearity between the constituent concentrations of the two endmember waters.

## 1.2 Field area

### 1.2.1 The Thau and its catchment

The Thau (Figure 1) is located on the Mediterranean coast (Hérault). With an area of  $75 \text{ km}^2$ , it is the largest of a series of coastal lagoons in France. It has a total watershed catchment of approximately  $280 \text{ km}^2$  (Plus et al. 2006), the geology of which is dominated by karstic limestones in the northeast and marls in the southwest (Figure 2).

Several rivers and streams feed into the Thau. The rivers whose catchment area is greater than 10% of the total lagoon watershed are shown in Table 1 (Plus et al. 2006). The Vène feeds into the crique de l'Angle (Angle cove) and is sourced by two intermittent springs flowing from Jurassic karst aquifers: the

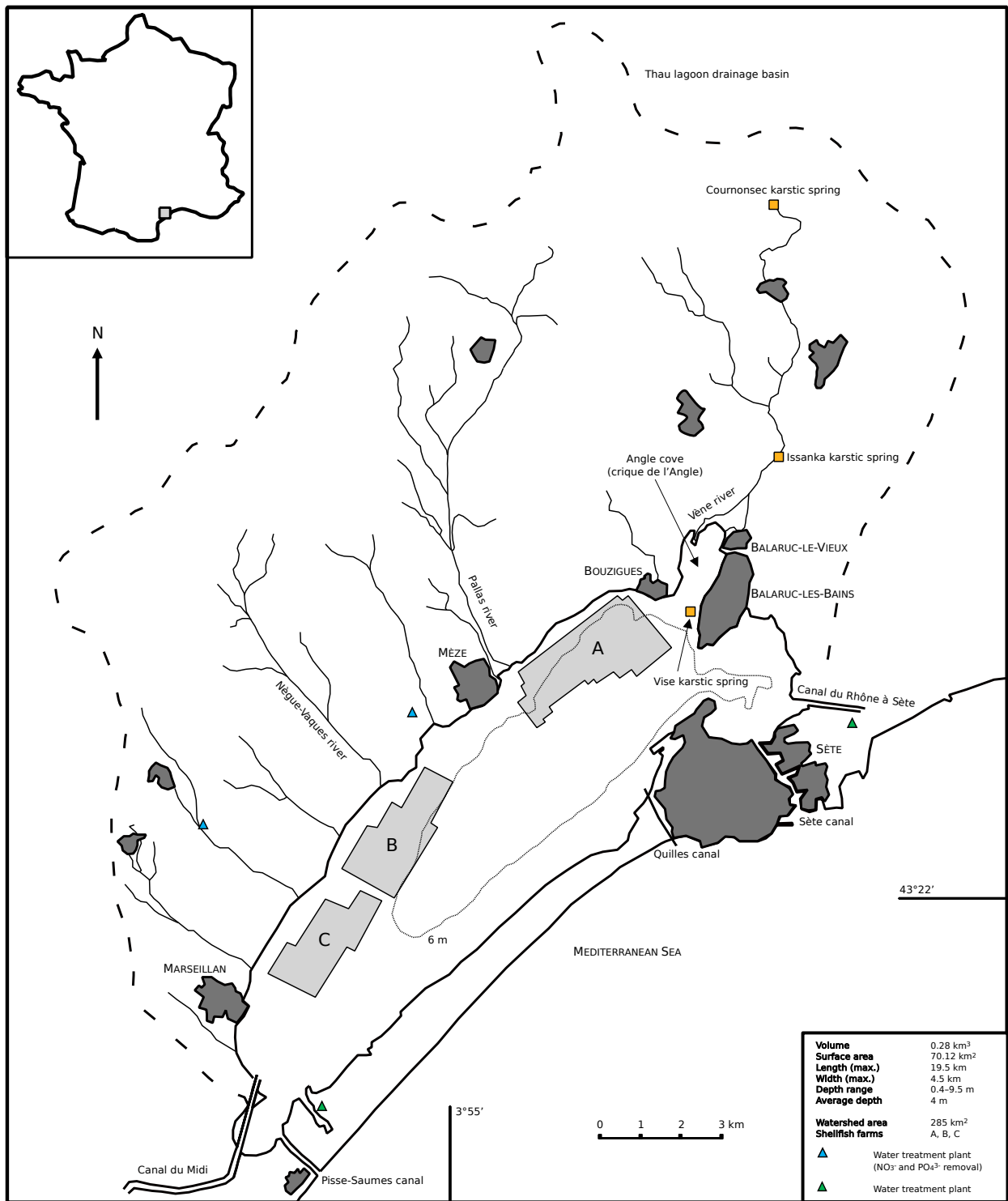


Figure 1: Overview map of the Thau lagoon. Adapted from (Jouffre and Amanieu 1991).

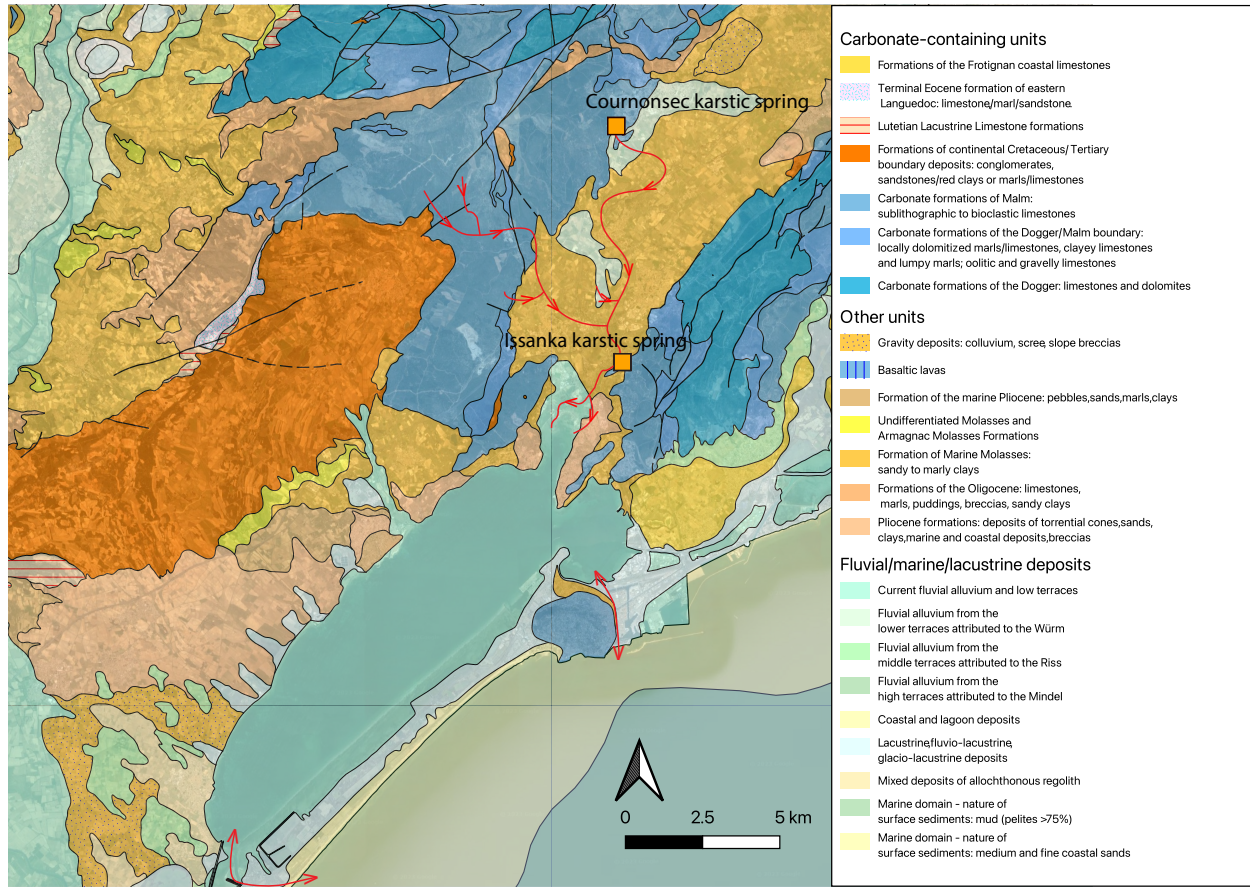


Figure 2: Lithology of the field area showing Vène flow path and the lagoon openings to the Mediterranean Sea. The karstic springs feeding the Vène are shown in orange. Geological data provided by BRGM under Open Licence Etalab Version 2.0. Map data ©1984 Google

Cournonsec and Issanka. The Thau connects to the Mediterranean Sea by a system of canals in Sète in the east, and at the Pisso-Saume canal in the southwest. The lagoon is also connected to the Hérault river in the southwest by the Canal du Midi, and to the Rhône river in the east by the Canal du Rhône à Sète. The Mediterranean climate is characterised by a low level of precipitation that is almost entirely concentrated between September and March. The Vène river shows high flow rates in these months with negligible flow rates during the remaining months (Plus et al. 2006; Obermann, Rosenwinkel, and Tournoud 2009; Obermann, Froebrich, et al. 2007) (Figure 3).

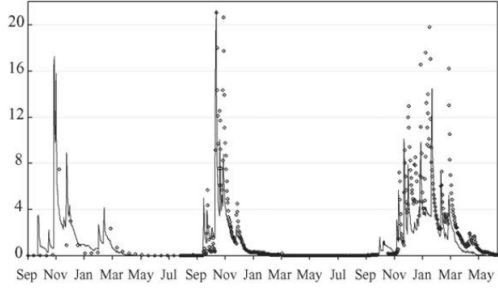


Figure 3: Measurements of Vène river flow rates from September 1993 to July 1996. Figure taken from (Plus et al. 2006).

River	Catchment area (%)
Vène	26
Pallas	21
Nègue-Vagues	13

Table 1: The major rivers that flow into the Thau. The percentages are the river catchment areas as a proportion of the total lagoon catchment area. Data taken from (Plus et al. 2006).

The submarine freshwater Vise spring is located in a 30 m depression (the deepest point of the lagoon) and is sourced by a limestone karst aquifer (*Dem'Eaux Thau* 2024; Ladouche et al. 2023). Its circular plume (Figure 4) was visible at the surface of the lagoon.

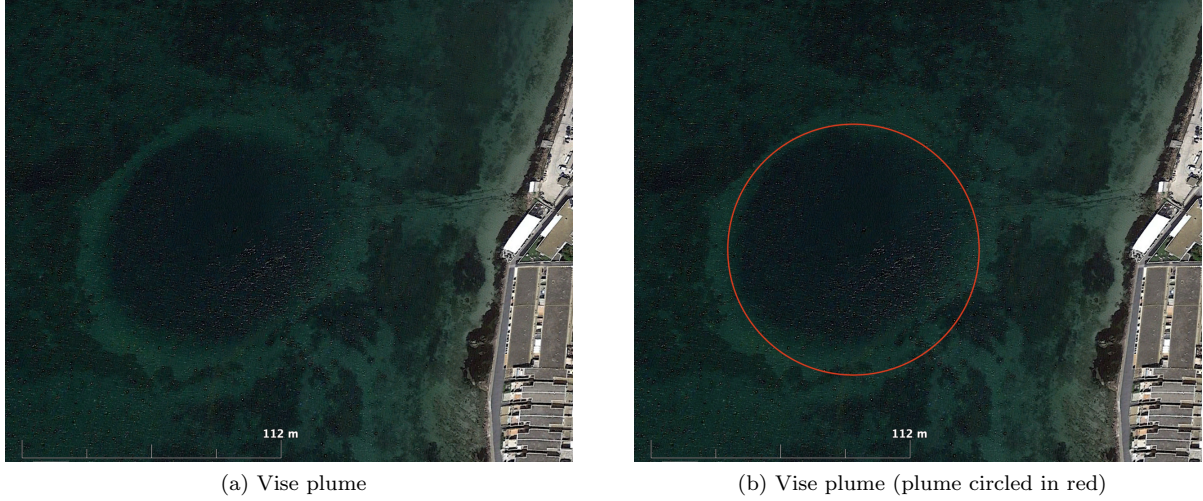


Figure 4: Satellite imagery of Vise plume. Map data ©2022 Google (image taken 04/2022). A plume similar to this was observed during fieldwork.

A land-cover map of the Thau catchment area (Figure 5) shows that the north of the Thau is predominantly agricultural, with the flow paths of the freshwater inputs to the Thau passing through vineyards. The remainder is garrigue, a form of low-growing shrub vegetation which grows on limestone soil (“Garrigue” and “Maquis” — *Parc national des calanques* 2023).

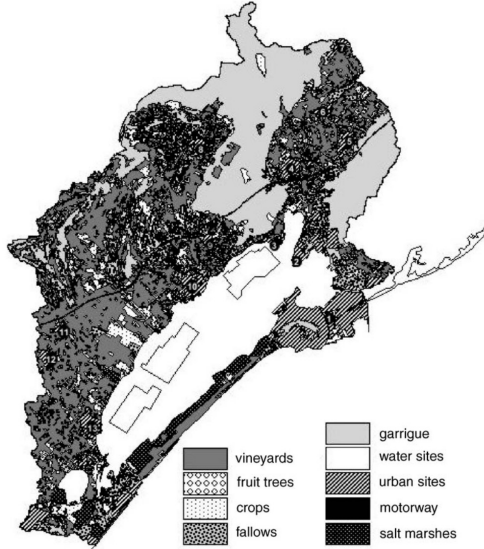


Figure 5: Land cover (1996) taken from (Plus et al. 2006).

### 1.2.2 Geography

The largest settlement around the lagoon is Sète. Other settlements include Balaruc-les-Bains, Balaruc-le-Vieux, Bouzigue, Mèze, Marseillan and small communities around the lagoon.

Shellfish farming is an important regional economic activity that occurs year-round in large farms in the north of the lagoon. Approximately 13,000 tonnes of oysters and 8,000 tonnes of mussels are produced annually, accounting for approximately 9% of French national production (*Oysters and mussels* 2023). The large shellfish populations in these farms produce  $\text{NH}_4^+$  via direct regeneration by excretions and indirect regeneration by bacterial degradation (mineralisation) of faeces and pseudofaeces in the sediments, producing over three times higher  $[\text{NH}_4^+]$  in the water column near the farms compared to the rest of the lagoon (Picot et al. 1990).

### 1.2.3 Residence time

Seawater flux from the Mediterranean Sea accounts for 95 % of the total water input to the Thau (Frenod 2013). Estimates of the residence time of waters in the Thau range from 50 to 200 days (Trombetta et al. 2021; Mesnage et al. 2007; Bacher, Bioteau, and Chapelle 1995). Because of its weak tidal range, the Thau's residence time mainly depends on wind and barometric effects (*Time Series: Thau Lagoon* 2024).

## 1.3 Initial Hypotheses

The initial hypotheses of this project were

1. The Vène is likely controlled by the lithology of the area, namely showing high alkalinity (Appendix A) along with  $[\text{Mg}^{2+}]$  and  $[\text{Ca}^{2+}]$  signatures characteristic of carbonate weathering.
2. Photosynthesis is likely ongoing in the Thau. Extensive photosynthesis would consume  $\text{NO}_3^-$ ,  $\text{NH}_4^+$  and  $\text{PO}_4^{3-}$ . Therefore, we would expect open lagoon water to be depleted in these compounds compared to inflowing waters. Furthermore, significant photosynthesis would be expected to increase alkalinity

and deplete total nitrogen and  $\text{PO}_4^{3-}$  in the extended 18:–16:–1 Redfield ratio. Previous literature suggests significant photosynthesis is occurring by siliceous centric diatoms (Vaulot 1986), so we would also expect the lagoon to be depleted in Si compared to inflowing waters.

3. Evaporation is likely ongoing in the Thau due to its temperate climate, shallow depth and relative enclosure from the Mediterranean Sea. Extensive evaporation would be expected to increase alkalinity, decrease pH and cause degassing of  $\text{CO}_2$ .
4. The waters at the Bouzigues shellfish farms likely show a higher  $[\text{NH}_4^+]$  than the rest of the lagoon due to biodeposition by shellfish. In June 1990, (Picot et al. 1990) found a spatial gradient of  $>1.5 \mu\text{mol l}^{-1}$   $\text{NH}_4^+$  at the farms compared to  $<0.5 \mu\text{mol l}^{-1}$  elsewhere in the lagoon. With continued shellfish farming in the three decades since this study, it was expected that a similar or stronger gradient in  $[\text{NH}_4^+]$  would be observed across the Thau.
5. As a karstic freshwater spring, the Vise likely shows a three-dimensional plume structure of low salinity and high alkalinity.

#### 1.4 Logistics

Fieldwork was carried out in late September with Giovanni Bernardi and Xianzhen Lin between 14/09/23 and 30/09/23 with one rest day on 22/09/23 during which no fieldwork was performed. Fieldwork was predominantly carried out in the northeast of the Thau interior.

## 2 Methods

### 2.1 Data collection and analysis

Samples were collected at the water surface unless otherwise stated. An HI-991300N pH probe was used to measure the pH, total dissolved solids (TDS), conductivity and temperature of the samples, and a salinity meter was used to measure the salinity. The collected samples were filtered through 0.2 µm filters and stored in plastic bottles at room temperature.

Titrations were performed using the Gran titration method. Samples were titrated using an initial volume of 0.05 N HCl of either 25 or 12.5 ml.

Spectrophotometry was performed using a D1900 spectrophotometer. The analytes tested by spectrophotometry were:  $\text{NO}_3^-$ -N as a proxy for  $\text{NO}_3^-$  (Appendix B.5),  $\text{PO}_4^{3-}$ ,  $\text{SiO}_2$ ,  $\text{NH}_3$ -N as a proxy for  $\text{NH}_4^+$  (Appendix B.6) and Cd.

Nineteen water samples (Table 2) were analysed using inductively coupled plasma optical emission spectrometry (ICP-OES) by Professor Ed Tipper and ion chromatography (IC) by Professor Sasha Turchyn in Cambridge against independent standards.

### 2.2 Analyte Rationale

pH, TDS, conductivity, temperature and salinity were measured to select samples for further testing based on hypotheses.

Alkalinity was measured to test whether there were significant effects of lithology, evaporation and photosynthesis in the field area, all of which were expected to increase alkalinity.

Si was measured to assess whether there was significant photosynthesis in the Thau by siliceous microorganisms (diatoms). Diatom growth was expected to deplete Si.

$\text{NO}_3^-$ ,  $\text{NH}_4^+$  and  $\text{PO}_4^{3-}$  were measured to test whether there was significant photosynthesis in the field area. Photosynthesis was expected to take up these nutrients according to the Redfield ratio.  $\text{NH}_4^+$  was also measured to test whether the shellfish farms produced significant  $\text{NH}_4^+$ .

Cd was measured as a corroborating test of diatom growth (Lane and Morel 2000). However, the few Cd tests performed returned negative results and hence further Cd testing was discontinued. The Cd results are not reported here.

### 2.3 Uncertainty

Equipment precision was calculated in the following manner:

1. A standard sample was repeatedly measured.
2. The sample mean ( $\bar{x}$ ) and sample standard error of the mean ( $\hat{\sigma}_m$ ) were used to define a normal distribution. Normality was tested for using the Shapiro-Wilk test.
3. A 95 % confidence interval (precision estimate) was constructed from this normal distribution.

When a field sample was measured multiple times, those field measurements were used to determine  $\bar{x}$  and  $\hat{\sigma}_m$  instead of the standard sample.

Accuracy was measured as a percent error, given by

$$\text{Percent error (\%)} = \frac{\bar{x} - (\text{accepted value})}{(\text{accepted value})} \times 100$$

A known reference sample was only available for pH/salinity probe data spectrophotometry data; therefore, precision alone was often used as a measure of uncertainty for the remaining analyte data.

Detailed spectrophotometry uncertainty data are shown in Appendix B.

## 2.4 Normalised inorganic charge balance

The normalised inorganic charge balance (NICB) of a water sample is given by

$$\text{NICB (\%)} = \frac{\sum^+ - \sum^-}{\sum^+ + \sum^-} \times 100$$

Where  $\sum^+$  is the sum of cations and  $\sum^-$  is the sum of anions, both in Eq1<sup>-1</sup>. The quality of water chemistry data may be assessed by its NICB. This is because water cannot hold a charge and so must have NICB = 0 %; deviations from NICB = 0 % result from major ion constituent measurement uncertainty. Table 2 shows the NICB for samples analysed in Cambridge. Based on project supervisor discussions, samples with  $|\text{NICB}| > 10 \%$  were treated with caution, and samples with  $|\text{NICB}| > 20 \%$  were removed from the results.

Sample	Location	NICB (%)	Sample	Location	NICB (%)
BOU-2809-01	Bouzigues	5.5	LVI-2509-02	Vène river	-1.4
BOU-2809-05	Bouzigues	5.9	LVI-2509-03	Vène river	6.9
CDL-2509-03	Angle cove	<b>24.6</b>	LVI-2509-04	Vène river	0.2
CDL-2509-05	Angle cove	8.9	LVI-2509-05	Vène river	8.9
CDL-2909-01	Angle cove	8.0	LVI-2909-04	Vène river	-2.4
CDL-2909-02	Angle cove	5.5	LVI-2909-05	Vène river	8.9
LVI-1909-05	Vène river	<b>15.0</b>	MED-2609-01	Mediterranean Sea	5.5
LVI-2109-07	Vène river	<b>11.2</b>	NVR-2709-01	Nègue-Vaques river	<b>42.3</b>
LVI-2509-01	Vène river	-2.2	VIS-2609-01	Vise spring	6.4
EVI-3009	N/A	<b>38.9</b>			

Table 2: NICB of samples analysed in Cambridge by ICP-OES and IC. Samples with  $|\text{NICB}| > 10 \%$  (shown in bold) were treated with caution. Samples with  $|\text{NICB}| > 20 \%$  were excluded from results. Note that EVI-3009 is a bottled water sample and does not appear in any figures.

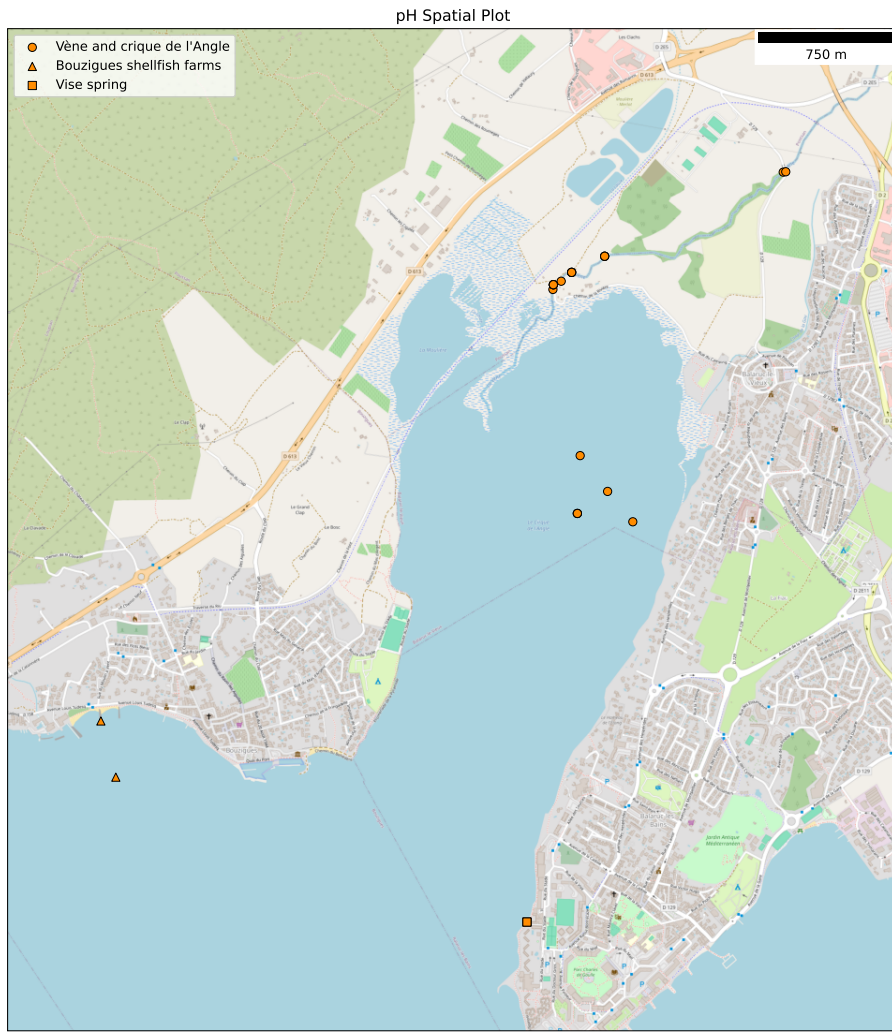


Figure 6: Positions of samples collected for ICP-OES and IC analysis. The notation of using circles for Vène and Angle cove samples, triangles for Bouzigues samples and squares for Vise and Nègue-Vaques samples is used throughout this report.

### 3 Results

See Appendix C for data table. Gran plots for titrations are supplied in the accompanying memory stick.

During fieldwork, the Pallas river had backfilled with lagoon water. Therefore, the Vène was considered to be the only river feeding the Thau, and hence all significant watershed inputs to the Thau were considered to be transported by the Vène.

#### 3.1 Lithological control on aqueous geochemistry

A cross-plot of  $\text{Na}^+$ -normalised  $\text{Mg}^{2+}$  and  $\text{Ca}^{2+}$  molar ratios (Figure 7) is used to assess the influence of water solute chemistry by lithology: the weathering products of silicates, carbonates and evaporites show characteristic  $\text{Na}^+$ -normalised  $\text{Mg}^{2+}$  and  $\text{Ca}^{2+}$  molar ratios due to their different mineral compositions. A conservative mixing line between the  $\text{Na}^+$ -normalised  $\text{Mg}^{2+}$  and  $\text{Ca}^{2+}$  molar ratio of Mediterranean water and the carbonate endmember from (Gaillardet et al. 1999) is shown.

#### 3.2 Alkalinity

Figure 8A shows an alkalinity–salinity cross-plot of water samples collected from the Vène and Thau. The Vène endmember for a theoretical conservative mixing line was calculated using the average alkalinities of three samples collected at the furthest upstream point accessible along the river. The alkalinity of the Thau endmember was estimated by simulating the evaporation of Mediterranean water (whose alkalinity was well constrained in the field) to hypersaline Thau water. In the field, the northeast Thau appeared to be almost uniformly saline at  $\sim 40$  ppt (Figure 9). This assumption was supported by ICP-OES analysis of samples from disparate regions of the interior of the lagoon (Table 3), which confirmed that the interior of the lagoon’s northeast is  $\sim 40.8$  ppt everywhere. The background alkalinity of northeastern lagoon water was therefore considered to be that of 9 % evaporated Mediterranean water. This assumption is justified because Thau water has an almost identical  $\text{Na}^+$ -normalised  $\text{Mg}^{2+}$  and  $\text{Ca}^{2+}$  molar ratio signature to the Mediterranean Sea (evaporation and dilution do not affect the  $\text{Na}^+$ -normalised  $\text{Mg}^{2+}$  and  $\text{Ca}^{2+}$  molar ratio signature of a water parcel); this similarity is not surprising, given the lagoon openings to the Mediterranean provide 95 % of the water flux to the lagoon (Frenod 2013).

Sample	Location	Salinity (ppt)
BOU-2809-01	Bouzigues	41.17
BOU-2809-05	Bouzigues	40.79
CDL-2909-02	Angle cove	40.81
VIS-2609-01	Vise spring	40.48

Table 3: Salinities (determined by ICP-OES) of samples from disparate locations in the northeast Thau.

#### 3.3 Si

Figure 10A shows an Si-salinity cross-plot of field and ICP-OES data from the Vène and Thau. The field data for the Vène freshwater and Mediterranean have again been used to constrain the theoretical conservative mixing line between the fresh Vène waters and the Thau. A simulation of 9 % evaporation of the field-determined Mediterranean [Si] lies close to actual field data collected in Bouzigues, suggesting such an evaporation simulation is valid. However, the Mediterranean [Si] determined by ICP-OES was

$-11.9 \mu\text{mol l}^{-1}$ , suggesting trace or no Si in the Mediterranean Sea. Many field data lie below the conservative mixing line, which may be due to inaccurate/imprecise field measurements. The ICP-OES data confirm the inaccuracy of the field data, suggesting a higher [Si] freshwater endmember and steeper conservative mixing line. However, there is broad agreement in the Si trends between the field and ICP-OES data.

### 3.4 $\text{NH}_4^+$

Despite its spectrophotometry test losing up to 30% sensitivity due to the high  $[\text{Cl}^-]$  of the samples, the  $[\text{NH}_4^+]$  broadly followed a trend of decreasing  $[\text{NH}_4^+]$  with increasing salinity (Figure 11A). The data show higher  $[\text{NH}_4^+]$  in the shore waters near the Vise spring and at the shore of the Mediterranean coast compared to the  $[\text{NH}_4^+]$  observed at the Bouzigues oyster farms. Furthermore, the sample collected at 4 m depth near an active shellfish farm showed higher  $[\text{NH}_4^+]$  than those samples collected at the surface.

### 3.5 $\text{NO}_3^-$

Figure 12A shows  $\text{NO}_3^-$  data from field and IC analysis. IC samples that are not shown were below detection level. The data show a clear gradient of decreasing  $[\text{NO}_3^-]$  with increasing salinity. The field  $[\text{NO}_3^-]$  data were systematically lower than the IC data. This is explained by the strong interference of  $\text{Cl}^-$  on the  $\text{NO}_3^-$ -N spectrophotometry test causing low results. However, the fresh Vène water likely had a lower  $[\text{Cl}^-]$  than the Thau water and hence was less strongly affected by this interference, if at all.

### 3.6 $\text{PO}_4^{3-}$

The field  $[\text{PO}_4^{3-}]$  data (Figure 13A) showed slightly higher  $[\text{PO}_4^{3-}]$  in the Vène than in the Angle cove; however, this trend was not significant given the  $\pm 1.5 \mu\text{mol l}^{-1}$  confidence interval. There appeared to be significantly higher  $[\text{PO}_4^{3-}]$  at certain points in the lagoon; however, it is not clear whether these were outliers or evidence of non-conservative behaviour.

### 3.7 Vise salinity

The Vise plume (Figure 14) showed an average salinity of 42.6 ppt extending down to 7m depth (Figure 16). This was more saline than the 39.7 ppt shore sample.

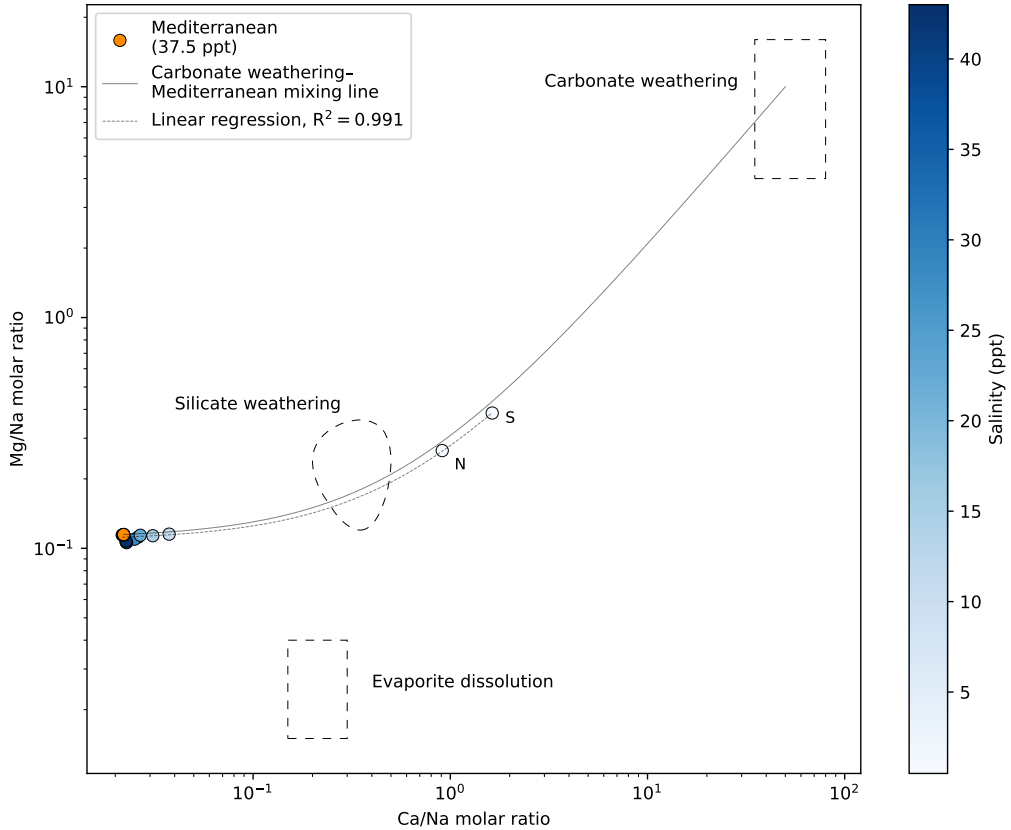


Figure 7: Cross-plot of  $\text{Na}^+$ -normalised molar ratios of  $\text{Mg}^{2+}$  and  $\text{Ca}^{2+}$  for samples analysed by ICP-OES. The Mediterranean sample analysed by ICP-OES is coloured orange and is almost identical to estimates of Mediterranean ion compositions by (Gaillardet et al. 1999; Gieskes 1998). Characteristic solute chemistry signatures of silicate, carbonate and evaporite weathering products from (Gaillardet et al. 1999) are shown. The curved appearance of the linear mixing and regression lines arises from plotting on log-log scales and is not a feature of the data.

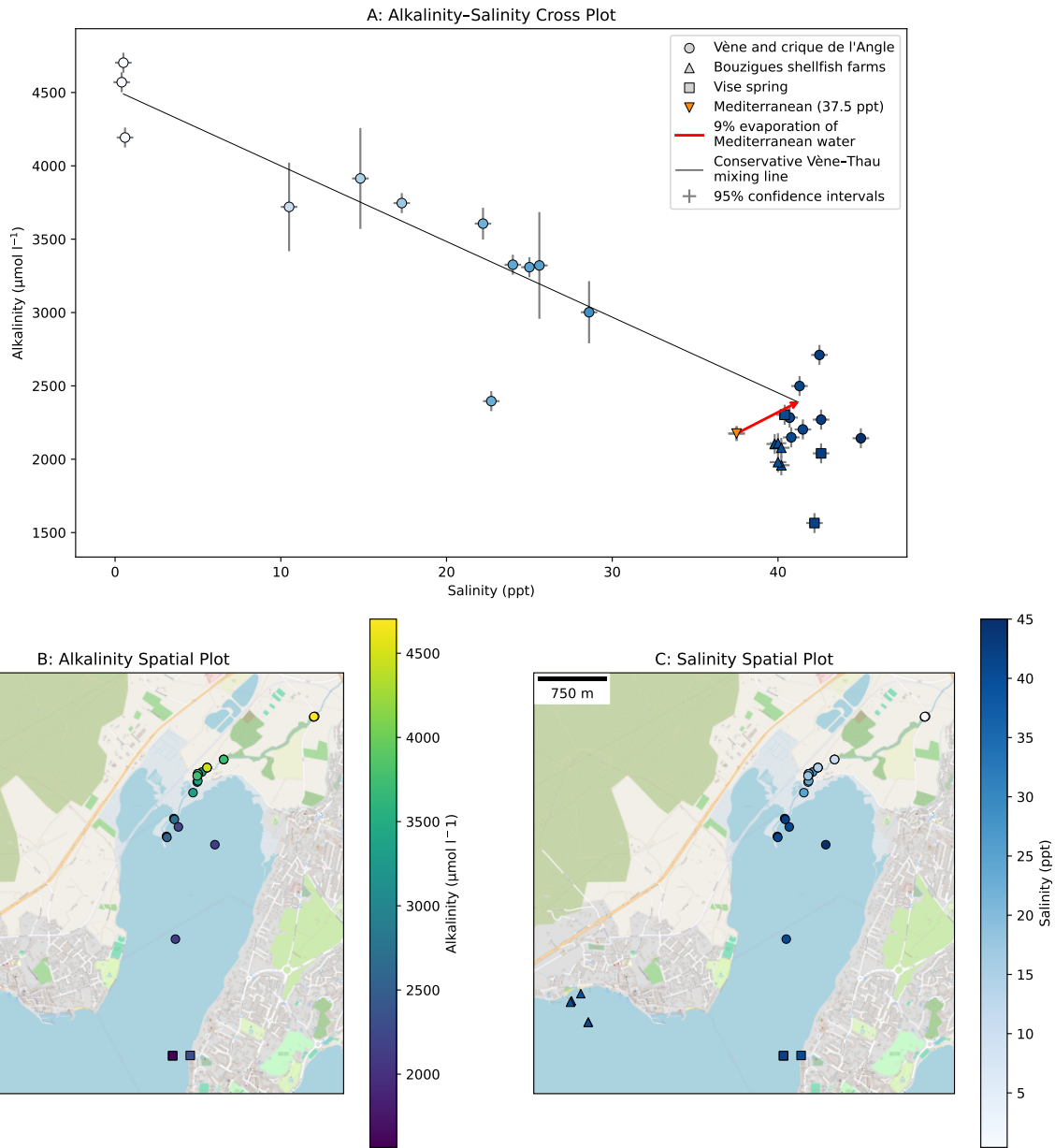


Figure 8: A: Cross-plot of salinity and alkalinity in the Vène and crique de l'Angle. The data are coloured by salinity for reference with C. The 9 % evaporation vector (red) shows the increase in alkalinity associated with the evaporation of 37.5 ppt Mediterranean water to 40.8 ppt Thau water B: Spatial plot of alkalinity in the Vène and Thau C: Spatial plot of salinity in the Vène and Thau.

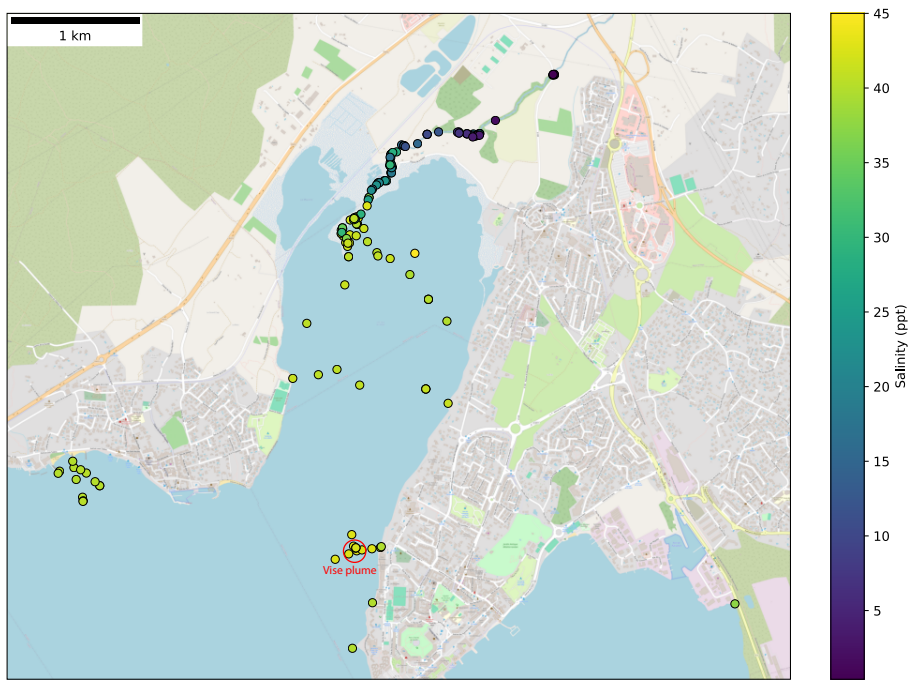


Figure 9: Salinity of the northeast Thau determined by salinity probe. The interior of the Thau. The Vise plume is shown in red.

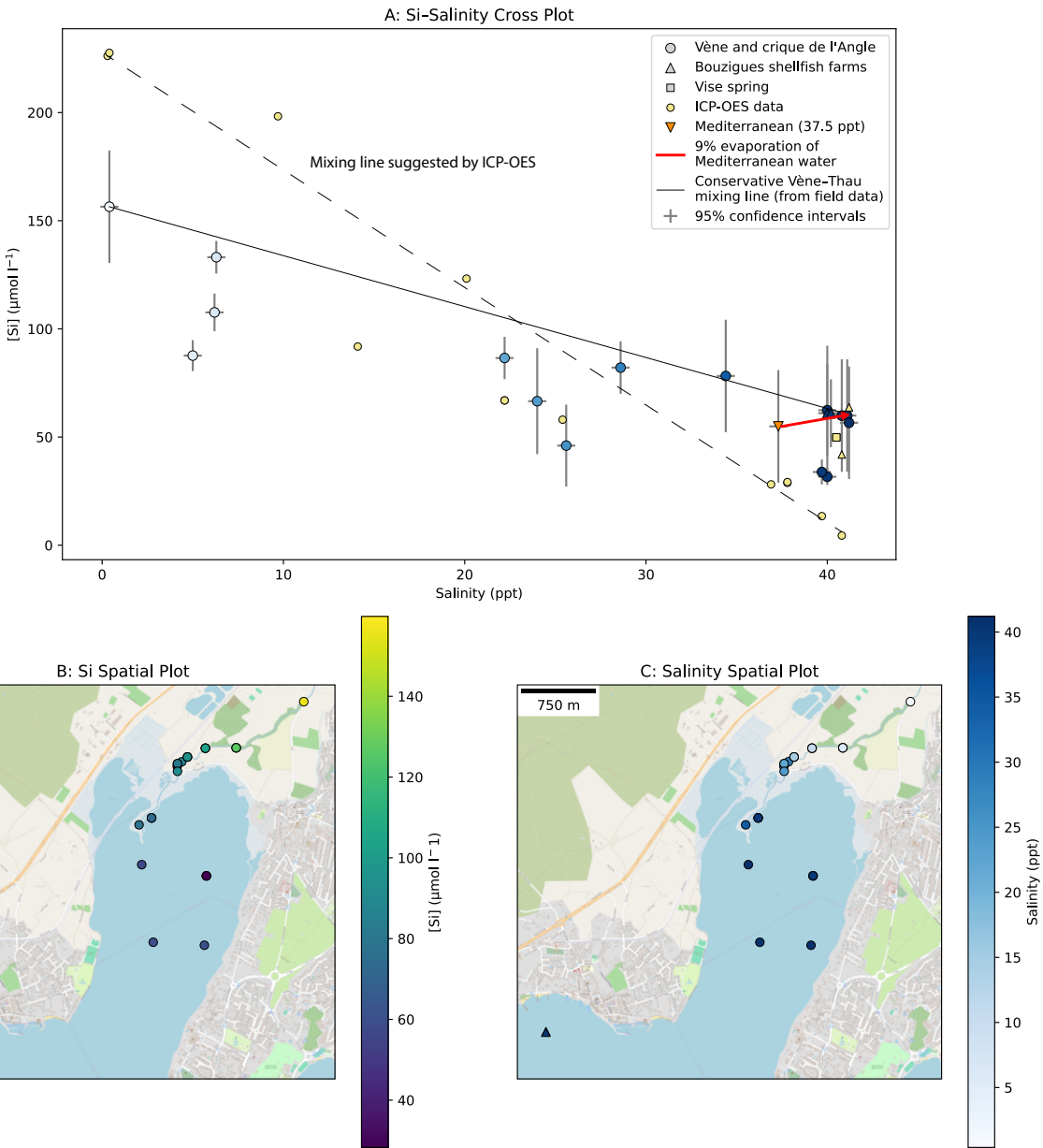


Figure 10: A: Cross-plot of salinity and  $[Si]$  in the Vène and Thau. The data are coloured by salinity for reference with C. The 9 % evaporation vector (red) shows the increase in  $[Si]$  associated with the evaporation of 37.5 ppt Mediterranean water to 40.8 ppt Thau water B: Spatial plot of  $[Si]$  in the Vène and Thau C: Spatial plot of salinity in the Vène and Thau.

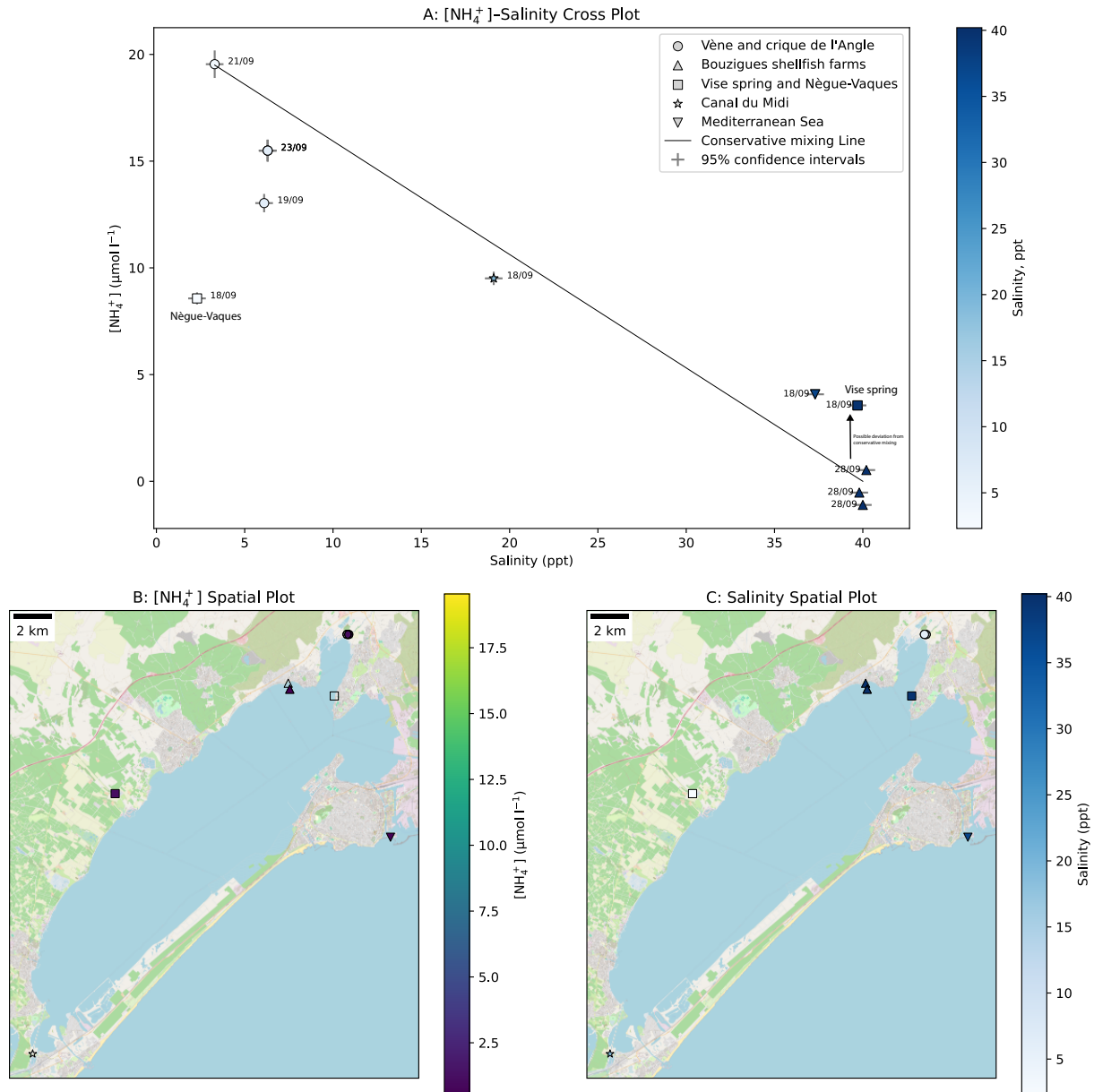


Figure 11: A: Cross-plot of salinity and  $[\text{NH}_4^+]$  in the Vène and Thau. The data are coloured by salinity for reference with C. An uncertainty of  $[\text{NH}_4^+]$  of  $\pm 3.3\%$  is shown (Appendix B.6). The sample collection date is shown (day/month) B: Spatial plot of  $[\text{NH}_4^+]$  in the Vène and Thau C: Spatial plot of salinity in the Vène and Thau.

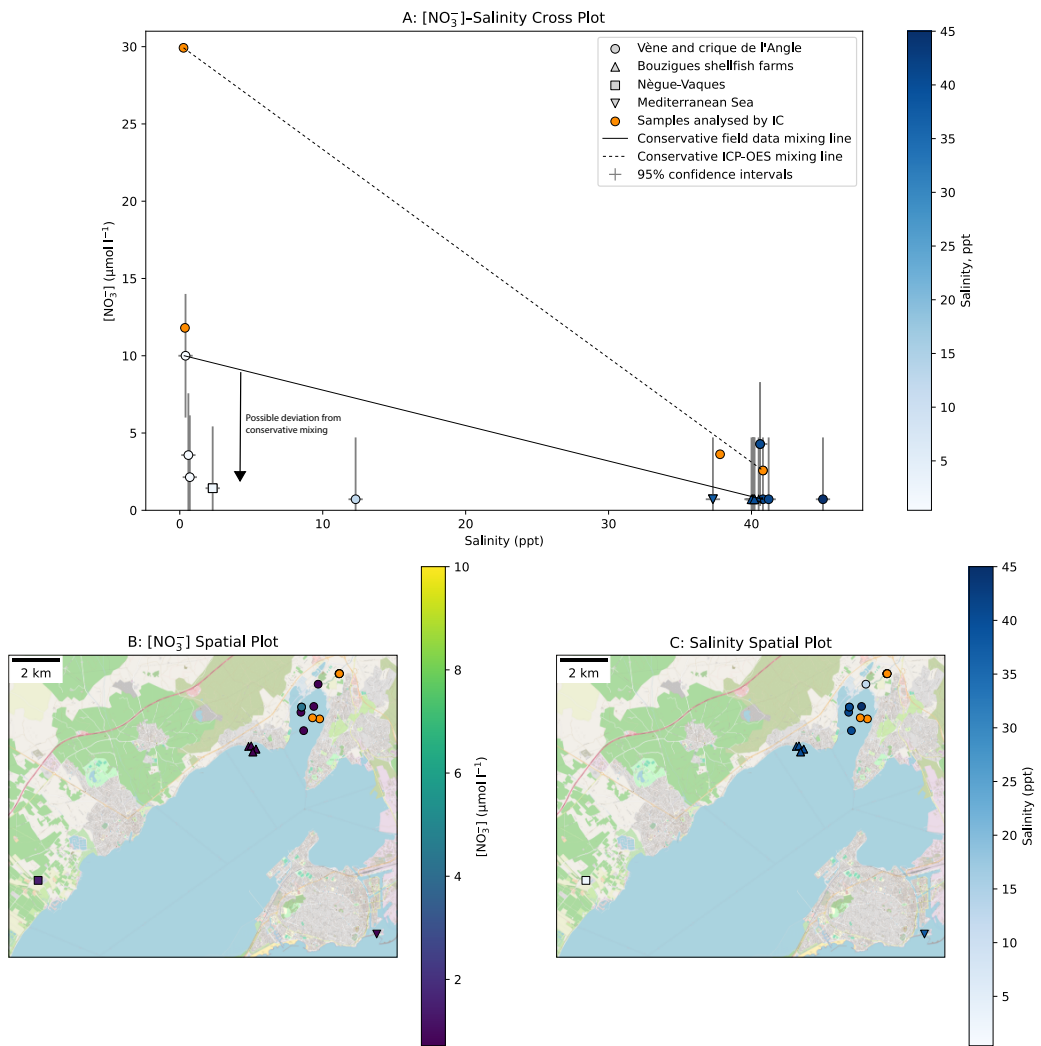


Figure 12: A: Cross-plot of salinity and  $[\text{NO}_3^-]$  in the Vène and Thau. The data are coloured by salinity for reference with C B: Spatial plot of  $[\text{NO}_3^-]$  in the Vène and Thau C: Spatial plot of salinity in the Vène and Thau.

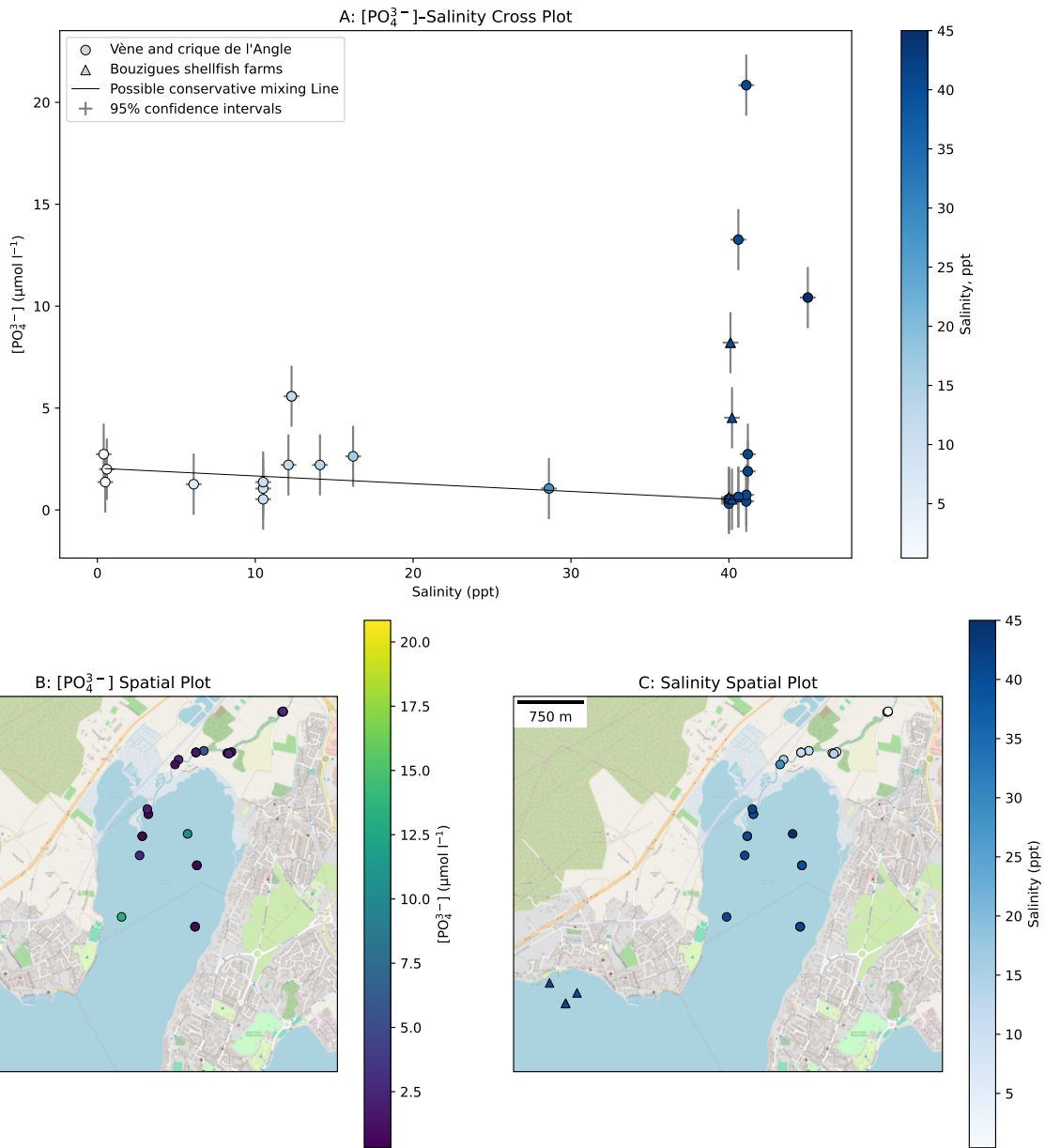
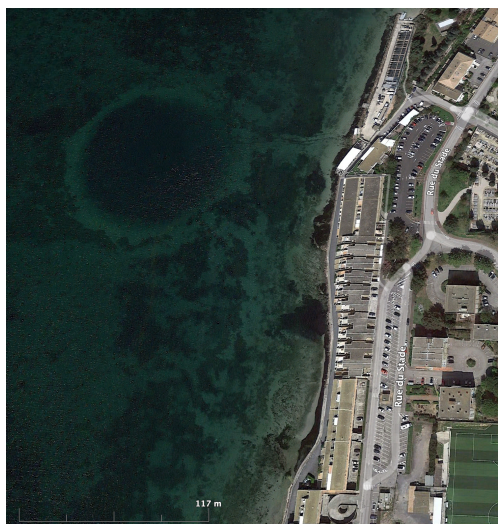
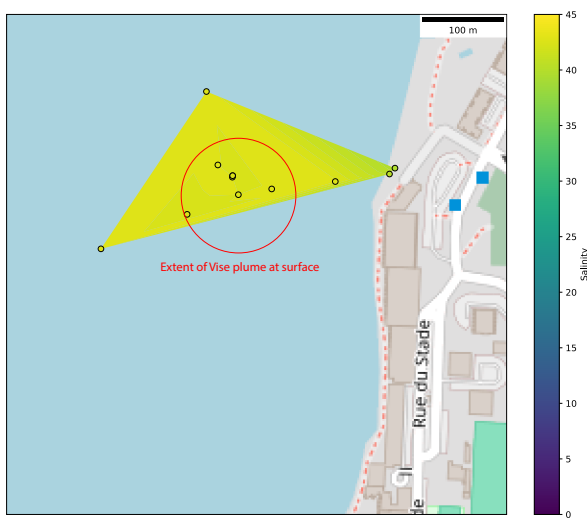


Figure 13: A: Cross-plot of salinity and  $[\text{PO}_4^{3-}]$  in the Vène and crique de l'Angle. The data are coloured by salinity for reference with C B: Spatial plot of  $[\text{PO}_4^{3-}]$  in the Vène and Thau C: Spatial plot of salinity in the Vène and Thau. A  $[\text{PO}_4^{3-}] = 126.9 \mu\text{mol l}^{-1}$  outlier has been excluded.



(a) Map data ©2022 Google (image taken 04/2022)



(b)

Figure 14: A: Satellite imagery and B: interpolated salinity map across the Vise plume (plume extent shown in red).

## 4 Discussion

### 4.1 Lithological control on aqueous geochemistry

The solute chemistry of the freshwater  $\text{Na}^+$ -normalised  $\text{Mg}^{2+}$  and  $\text{Ca}^{2+}$  molar ratios (Figure 7) show an influence of carbonate weathering because of the Vène's sources from karstic springs. This hypothesis is supported by both samples lying extremely close to the conservative mixing line between the carbonate weathering and seawater endmember. Freshwater samples S and N were collected at the same location yet show different  $\text{Na}^+$ -normalised  $\text{Mg}^{2+}$   $\text{Ca}^{2+}$  molar ratio signatures. One hypothesis is that this is due to wind-forcing: the Vène flow rate was observed to be extremely slow during fieldwork, and appeared to respond strongly to wind-forcing. Sample S was collected when the prevailing wind direction blew southwards, wind-forcing water with a stronger carbonate signature downstream. In contrast, sample N was collected when the prevailing wind direction blew northwards, wind-forcing Thau water upstream. Salinity maps of the Vène on these days (Figure 15) support this hypothesis, showing the shifted position of the mixing interface on days of different prevailing wind direction. Note that both of these samples had NICB > 10 %, so some of this observed variance in molar ratios may instead be due to ICP-OES inaccuracy. Although the Cournonsec and Issanka springs were inaccessible, their waters likely have a solute chemistry further towards the carbonate endmember than these samples, given they are sourced from carbonate rocks.

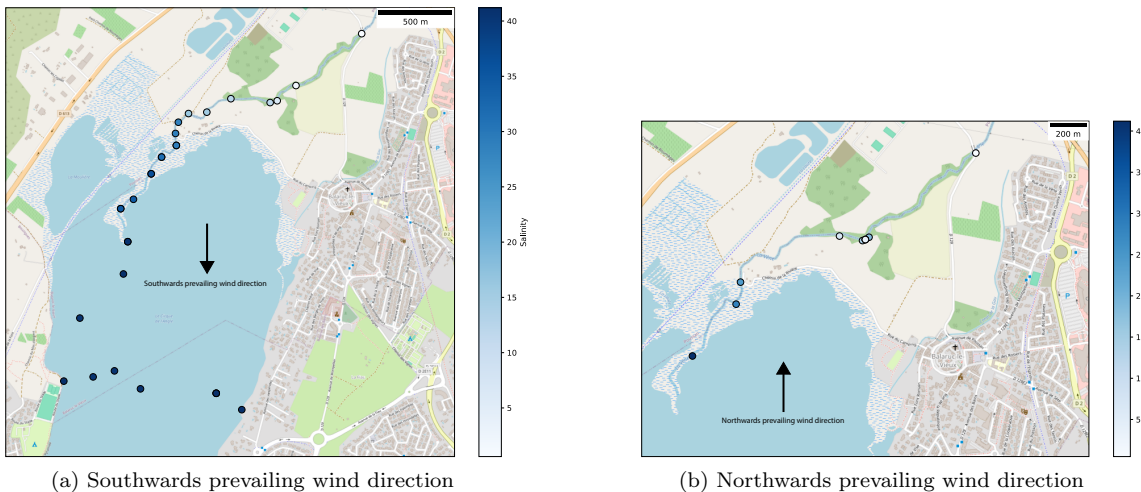


Figure 15: Salinity maps of the Vène and Angle cove on A: 19/09/23 (southwards prevailing wind direction) and B: 21/09/23 (northwards prevailing wind direction). Note the shifting position of the mixing interface between fresh and saline waters between days.

Figure 7 shows no effect of evaporite dissolution in the Thau. This is expected because evaporite precipitation which begins at approximately 50 % evaporation of seawater as opposed to the ~9 % found here.

### 4.2 Evaporation

Aside from outliers at 22.7 and 45.0 ppt, the alkalinity data (Figure 8) broadly follow the theoretical conservative mixing line, implying conservative mixing between the Vène and Thau. However, there appears to be significant variance in alkalinity of hypersaline lagoon water; this variance may be due to inaccurate/imprecise measurements, but may in part be due to evaporation.

Evaporation must be occurring in the Thau: during the three months before the project, the lagoon received almost no precipitation so must have sourced its water almost exclusively from the 37.5 ppt Mediterranean Sea. Therefore, it must have evaporated to reach its observed  $\sim 40.8$  ppt. Figure 9A shows the direction points move in salinity-alkalinity space during evaporation. The hypersaline points appear to broadly align with in the direction of this vector, suggesting they have evaporated. However, it is difficult to confirm whether samples align with this vector across such small salinity ranges.

To test whether these hypersaline points were showing alkalinity variance due to evaporation, the  $p\text{CO}_2$  values of samples collected in the northeast Thau were calculated using their salinity, pH, temperature and alkalinity values (Figure 16). Samples with  $p\text{CO}_2 > 420$  ppm degas  $\text{CO}_2$  to the atmosphere. The samples with higher alkalinity have a higher DIC (Appendix A) and so show greater  $p\text{CO}_2$ . Figure 16 shows the  $p\text{CO}_2$  and pH change expected for a sample of evaporated Mediterranean water. The hypersaline samples broadly align with these paths through  $p\text{CO}_2$ -salinity and pH-salinity space, providing evidence that the observed alkalinity variation is due to evaporation.

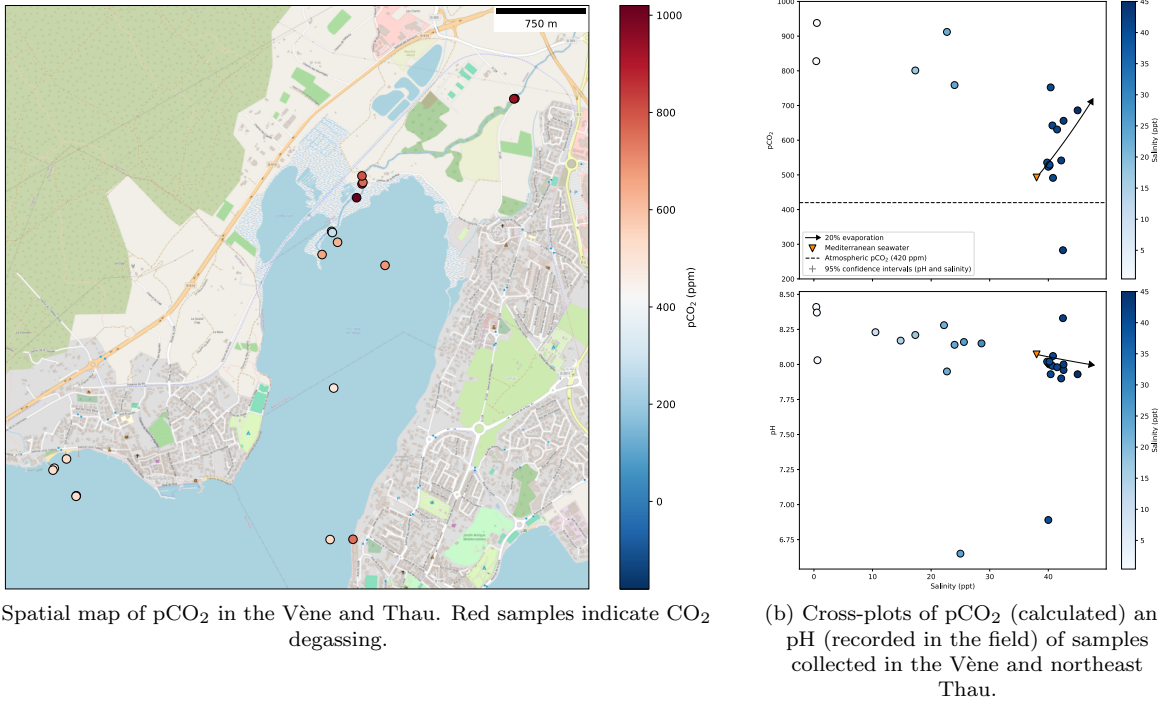


Figure 16: DIC speciation calculated using cbsyst under the MIT license.

The  $\text{CO}_2$  degassing observed in Figure 16 suggests another possible non-conservative process acting on alkalinity in the Vène and Thau:  $\text{CO}_2$  degassing can shift DIC towards  $\text{CO}_3^{2-}$ , causing it to become supersaturated in the water and precipitate as  $\text{CaCO}_3$ . This removal of  $\text{CO}_3^{2-}$  non-conservatively reduces alkalinity, and may have occurred in the Vène and Thau. However, it is difficult to distinguish the decrease in  $p\text{CO}_2$  and pH associated with  $\text{CaCO}_3$  precipitation from their decrease by conservative mixing, and the alkalinity data do not deviate significantly below the conservative mixing line. This suggests that despite its high  $p\text{CO}_2$ , significant  $\text{CaCO}_3$  precipitation has not occurred in the Vène or the Thau. It is likely that the rate of degassing is too slow to induce significant  $\text{CaCO}_3$  precipitation.

To test for diurnal influences on the alkalities of these hypersaline samples, their alkalinities were plotted

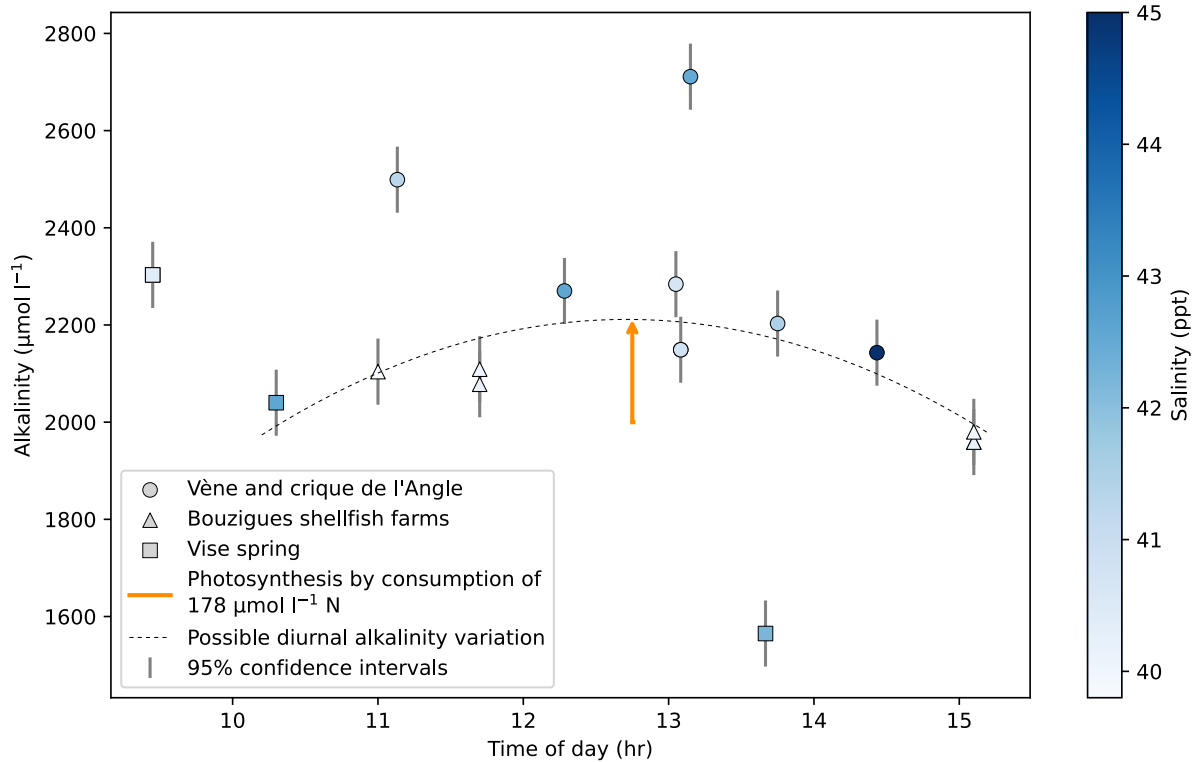


Figure 17: Cross-plot of alkalinity against time of collection showing a possible diurnal trend in alkalinity (dashed line).

against time of collection and coloured by salinity (Figure 17). There appears to be no significant increase in salinity during the day, and so a diurnal increase in alkalinity of lagoon waters by evaporation is unlikely.

Because the mixed water of intermediate salinity (10-30 ppt) does not deviate significantly from the conservative mixing line, the rate of Vène-Thau mixing is likely faster than the rate of evaporation of both waters, causing fresh Vène waters to mix and becoming indistinguishable from Thau waters before experiencing significant evaporation. Due to its relatively uniform salinity, the Thau is likely close to steady state with respect to its water inputs and outputs, meaning its salinity remains relatively constant with time.

### 4.3 Photosynthesis

Figures 11 and 12 support the hypothesis that significant photosynthesis has occurred in the Thau: the interior of the lagoon is depleted in these nitrogen compounds compared to the inflowing Vène water. The Vène likely sources its nitrogen compounds from agricultural runoff, given the significant land cover by vineyards in its watershed. This hypothesis is supported by the over two times lower  $[\text{NH}_4^+]$  in the Nègue-Vagues compared to the Vène, as the Nègue-Vagues has half of the watershed area as the Vène from which to source nitrogen compounds. The  $\text{NO}_3^-$  field data also show apparent non-conservative removal of  $\text{NO}_3^-$  in intermediate salinity waters. This may have been the result of photosynthesis occurring in these mixed waters. However, it is more likely due to the  $\text{Cl}^-$  interference on the  $\text{NO}_3^-$ -N test causing low results: The field  $[\text{NH}_4^+]$  for sample LVI-1909-05 was  $3.57 \mu\text{mol l}^{-1}$  whereas the  $[\text{NH}_4^+]$  by ICP-OES was  $29.9 \mu\text{mol l}^{-1}$ .

The lack of significant difference between  $[\text{PO}_4^{3-}]$  in the Vène and Thau (Figure 13A) further supports the

hypothesis that significant photosynthesis is responsible for the depletion of total nitrogen in the lagoon. Photosynthesis takes up 16 times less  $\text{PO}_4^{3-}$  than total nitrogen, and so would be expected to deplete total nitrogen in the Thau compared to the Vène, but leave  $[\text{PO}_4^{3-}]$  relatively unaffected between the Vène and Thau, as the observed data show. It is unlikely that there were  $>10 \mu\text{mol l}^{-1}$   $[\text{PO}_4^{3-}]$  variations in the relatively well-mixed waters of the Angle cove. Therefore, these significantly higher  $[\text{PO}_4^{3-}]$  are likely outliers, perhaps caused by contamination of the spectrophotometry test.

The alkalinity data (Figure 8) show broadly conservative mixing, suggesting that significant photosynthesis is not occurring on mixed waters

To verify whether there was a diurnal effect of photosynthesis on these hypersaline samples, their alkalinities were plotted against time of collection (Figure 11). There appeared to be a possible increase in alkalinity as sunlight increased during the day. This is consistent with the effect of photosynthesis on alkalinity: the consumption of  $\text{CO}_2$  associated with photosynthesis shifts DIC speciation towards  $\text{CO}_3^{2-}$ , increasing alkalinity. However, the data were very scattered, and the photosynthesis required to produce a  $200 \mu\text{mol l}^{-1}$  alkalinity increase would consume  $178 \mu\text{mol l}^{-1} \text{NO}_3^-$ .

However, Figures 11 and 12 confirm that the Thau is limited to  $3\text{--}8 \mu\text{mol l}^{-1}$  total nitrogen. Therefore, the  $178 \mu\text{mol l}^{-1}$  total nitrogen required to produce a diurnal increase of  $200 \mu\text{mol l}^{-1}$  alkalinity is not available. The Vène was observed to have a slow flow rate of estimated  $1 \text{ cm s}^{-1}$ , so it is unlikely that it was supplying significant  $\text{NO}_3^-$  and  $\text{NH}_4^+$  loads to the Thau to support such large hypothesised diurnal alkalinity trends.

To test whether significant photosynthesis had occurred by siliceous diatoms,  $[\text{Si}]$  was plotted against salinity (Figure 10). The field and ICP-OES Si data broadly agree with one another in their trends. Both show apparent conservative mixing; however, the ICP-OES data suggest a steeper mixing line that extends to a saline endmember of  $0 \mu\text{mol l}^{-1}$  Si. This suggests that significant Si depletion has occurred in the Thau. One possibility is that Si uptake by photosynthetic diatoms has occurred; this hypothesis is supported by the data showing the significant consumption of nitrogen compounds, and the Thau's connection to the Mediterranean Sea provides a means of supplying centric diatoms to the lagoon.

#### 4.4 Shellfish farming

There did not appear to be significant shellfish farming occurring during the project; a few farms were loaded with shellfish but many appeared empty. To test whether there was any evidence for biodeposition of  $\text{NH}_4^+$  by shellfish, three samples were taken at different locations relative to a loaded farm (Figure 18). These data show  $1.6 \mu\text{mol l}^{-1}$  higher  $[\text{NH}_4^+]$  at 4 m depth compared to the surface of the shellfish farm, supporting the hypothesis that shellfish produce  $\text{NH}_4^+$  by biodeposition in the water column. This  $[\text{NH}_4^+]$  increase in the shellfish farm water column is of a similar size to the one found by (Picot et al. 1990), suggesting shellfish biodeposition is the source of this  $\text{NH}_4^+$ . Note that the  $\text{Cl}^-$  interference on the  $\text{NH}_3\text{-N}$  test increased the uncertainty of the  $\text{NH}_4^+$  data.

Furthermore, while both  $\text{NO}_3^-$  and  $\text{NH}_4^+$  show depletion in the Thau compared to the inflowing Vène water, the data unexpectedly showed  $\sim 5 \mu\text{mol l}^{-1}$  higher  $\text{NH}_4^+$  at the shore near the Vise spring and at the Mediterranean coast than at the Bouzigues shellfish farms. The depleted  $\text{NO}_3^-$  observed in the lagoon interior suggests that watershed input of nutrients to the lagoon interior was not responsible for this higher  $\text{NH}_4^+$  observed near the Vise spring and Mediterranean Sea. Previous literature indicates that  $\text{NH}_4^+$  is the predominant form of inorganic nitrogen in anoxic sediments, produced by the decomposition of organic nitrogen

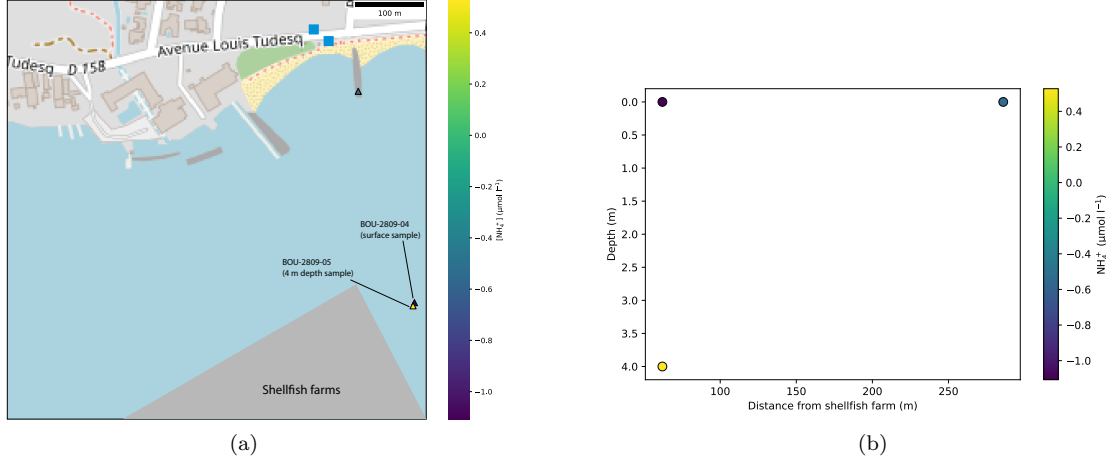


Figure 18: A: Spatial plot of  $\text{NH}_4^+$  at a site of active shellfish farming. Sample IDs and collection depths at the shellfish farm are shown. Negative values are taken to mean trace amounts of  $\text{NH}_4^+$ . B: Spatial plot of  $\text{NH}_4^+$  with depth in the water column and distance from shellfish farm.

compounds (Rosenfeld 1979). (Jouffre and Amanieu 1991) state that strong wind-forcing in the autumn causes resuspension of these sediments, causing  $\text{NH}_4^+$  release on the order of  $>4.2 \mu\text{mol l}^{-1}$ , particularly in shallow waters. This may explain the high  $[\text{NH}_4^+]$  observed outside of the deep waters characterising the Bouzigues shellfish farms. If this hypothesis is true, then wind-forcing plays a greater role in the nutrient distribution in the Thau than initially hypothesised and is a dominant control during the autumn. However, our spatial mapping of  $[\text{NH}_4^+]$  was low-resolution, and more sampling would need to be done in waters of different depths to confirm this sediment resuspension hypothesis. Typical  $[\text{NH}_4^+]$  distributions in the Thau during the summer and winter are shown in Figure 19.

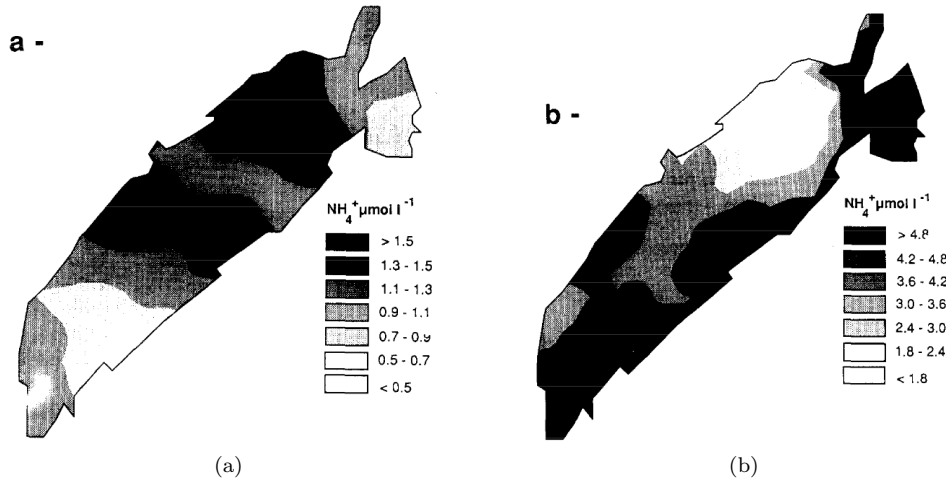


Figure 19:  $[\text{NH}_4^+]$  distributions in the Thau. Taken from (Picot et al. 1990). A: Summer distribution. Note the high  $[\text{NH}_4^+]$  at the shellfish farming sites along the north of the lagoon. B: Winter distribution. (Jouffre and Amanieu 1991) hypothesised that sediment resuspension by wind-forcing preferentially releases  $\text{NH}_4^+$  in the shallow waters of the lagoon.

## 4.5 Vise spring structure

It was hypothesised that the Vise spring would show a low-salinity plume structure. During fieldwork, the spring showed a circular plume feature at the surface of the water, supporting the hypothesis that there was a flowing plume structure present.

However, the plume was  $\sim 3$  ppt more saline than its surroundings (Figure 14). This result was unexpected, and it is unlikely that evaporation caused this salinity difference across  $\sim 100$  m of open water. Previous literature showed that the Vise is susceptible to *inversac* periods of a few weeks to several months, during which salty water intrudes into the spring conduit, causing salinisation of the underlying karst aquifer (Ladouce et al. 2023). Seven such events have occurred since the 1960s, with the last one occurring between 28/11/2020 and 14/03/2022; however, the factors responsible for them are not well understood (Pétré et al. 2020). It is likely that significant saltwater intrusion of the underlying karst aquifer occurred, resulting in our observations of plume water being more saline than shore water. This hypothesis is supported by the Vise spring samples showing similar alkalinities to the Thau, rather than the higher alkalinity expected from waters sourced from a karstic spring. Before the last *inversac* period, (Maréchal et al. 2022) reported a Vise outflowing rate of  $60\text{ l s}^{-1}$  which inverted to a backflow of  $\sim 350\text{ l s}^{-1}$  from the lagoon into the aquifer over a few minutes as the *inversac* began. A backflow rate of  $150\text{ l s}^{-1}$  was recorded a year after the *inversac* period began, supporting the hypothesis that a large reservoir of saline water was stored in the karst after the *inversac* period had finished, and that we were observing its outflow into the lagoon.

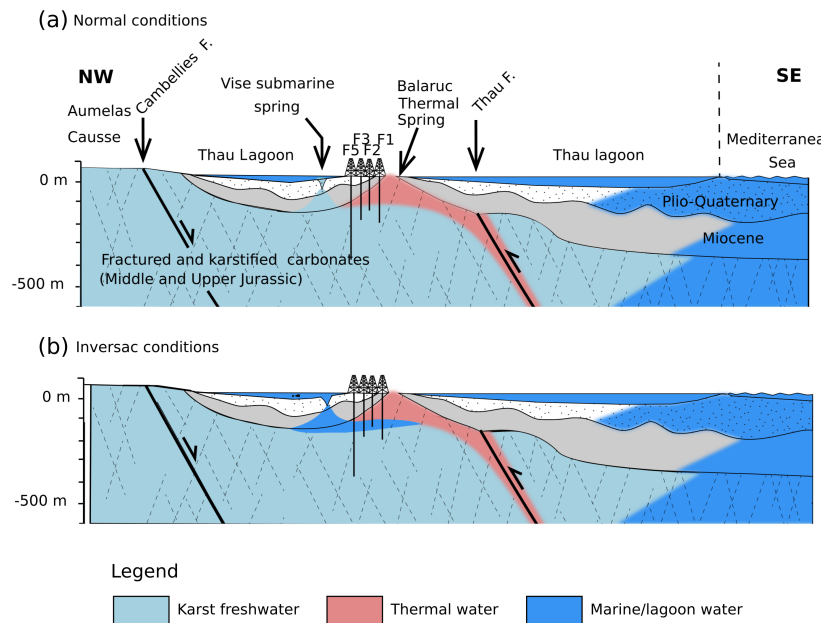


Figure 20: Schematic of flow reversal during *inversac* period. Figure taken from (Pétré et al. 2020)

## 5 Conclusions

The Vène is a freshwater river whose solute chemistry is strongly controlled by carbonate weathering products, showing a  $\text{Na}^+$ -normalised  $\text{Mg}^{2+}$  and  $\text{Ca}^{2+}$  molar ratio and high alkalinity typical of water sourced from a karstic limestone aquifer.

Extensive evaporation is occurring in the region: the Thau shares the same  $\text{Na}^+$ -normalised  $\text{Mg}^{2+}$  and  $\text{Ca}^{2+}$  signature as the Mediterranean Sea yet is hypersaline at  $\sim 40.8$  ppt, representing  $\sim 9\%$  evaporation of 37.5 ppt Mediterranean seawater. Significant evaporation was not occurring in the Vène because alkalinity and Si appeared to mix conservatively. This suggests that the rate of Vène-Thau mixing is faster than the rate of evaporation. This leads to the conclusion that most evaporation occurs in the Thau. This hypothesis is supported by observed non-conservative alkalinity change in the Thau, which total nitrogen data and  $\text{pCO}_2/\text{pH}$  calculations confirmed was likely due to evaporation rather than photosynthesis. It is also likely that no significant  $\text{CaCO}_3$  precipitation occurs in the Vène or Thau, despite both waters degassing  $\text{CO}_2$  to the atmosphere.

The Thau has experienced significant uptake of total nitrogen by photosynthesis. Vène water is rich in total nitrogen; however, its slow flow rate had not yet increased significantly since the summer, and so the Thau had not been recharged with  $\text{NO}_3^-$ . It is difficult to distinguish possible non-conservative uptake of  $\text{NO}_3^-$  by phytoplankton from the aforementioned  $\text{Cl}^-$  interference causing low spectrophotometry results.

Along with showing depletion in the Thau indicative of uptake by photosynthesis,  $\text{NH}_4^+$  shows higher concentrations in the water column beneath the Bouzigues shellfish farms compared to the surface, supporting the hypothesis that significant biodeposition of  $\text{NH}_4^+$  occurs there. Furthermore, areas of shallow water showed higher  $[\text{NH}_4^+]$  than at the Bouzigues shellfarms. Resuspension of  $\text{NH}_4^+$ -rich sediments is one explanation for this distribution and is supported by salinity maps showing the effect of wind forcing on water mass movement in the Vène.

Despite being a freshwater spring, the Vise showed higher salinity than the rest of the lagoon. It is likely that we observed the outflowing of saline lagoon water that had backfilled into the underlying Vise karst aquifer during its previous inversac period. This hypothesis is supported by Vise water showing a similar alkalinity to that of the Thau, rather than the high alkalinity expected of karstic spring water.

## A Alkalinity and DIC

The *total alkalinity* of a water sample is defined as the excess of bases over acids, and is operationally defined by the titration with H<sup>+</sup> of all weak bases present in solution (Sarmiento and Gruber 2006).

We define total alkalinity as

$$\text{Total alkalinity} = [\text{HCO}_3^-] + 2[\text{CO}_3^{2-}] + [\text{OH}^-] - [\text{H}^+] + [\text{minor bases}]$$

The pH of samples ranged from 7.61 to 8.46, so [H<sup>+</sup>] and [OH<sup>-</sup>] ranged from  $2.45 \times 10^{-2}$  to  $4.07 \times 10^{-1}$   $\mu\text{mol l}^{-1}$  and  $2.88 \times 10^{-2}$  to  $3.47 \times 10^{-3}$   $\mu\text{mol l}^{-1}$ , respectively. Therefore, in comprising the total alkalinity of our samples, these species contributed negligibly to the total alkalinities of our samples.

We define *carbonate alkalinity* as

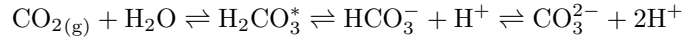
$$\text{Carbonate alkalinity} = [\text{HCO}_3^-] + 2[\text{CO}_3^{2-}]$$

which is functionally identical to total alkalinity when both were on the order of 1000  $\mu\text{mol l}^{-1}$  in this field area. Therefore, total and carbonate alkalinity are not distinguished in the text.

Dissolved inorganic carbon (DIC) is defined as

$$\text{DIC} = [\text{H}_2\text{CO}_3^*] + [\text{HCO}_3^-] + [\text{CO}_3^{2-}]$$

where CO<sub>2(aq)</sub> and H<sub>2</sub>CO<sub>3</sub> are grouped into the hypothetical H<sub>2</sub>CO<sub>3</sub><sup>\*</sup> due to the difficulty in analytically distinguishing between the two species. The speciation of DIC (the relative concentrations of each component carbonate species) depends on the position of the dynamic equilibrium of



which is strongly dependent on pH. If CO<sub>2(g)</sub> is removed or CO<sub>3<sup>2-</sup></sub> added, the dynamic equilibrium shifts to the left according to Le Chatelier's principle. However, the pH change by the H<sup>+</sup> consumption associated with this process causes a net shift in dynamic equilibrium to the *right*, shifting DIC speciation *towards* CO<sub>3<sup>2-</sup></sub>, *increasing* alkalinity. The opposite is true if CO<sub>2</sub> is added or CO<sub>3<sup>2-</sup></sub> removed.

Therefore, aqueous processes which produce or consume CO<sub>2</sub>, such as respiration and photosynthesis, produce a corresponding decrease or increase in alkalinity, respectively.

## B Uncertainty data

### B.1 Salinity and pH probe uncertainty

The accuracies of the salinity and pH probes decreased with time since calibration. However, their precisions remained unaffected. The accuracy and precision of the probes were calculated in the following manner:

1. Each morning, standard solutions for both probes (35 ppt and pH 7) were recorded, calibrated to and then rerecorded. The drifts in probe readings of these solutions over the previous 24 hours were recorded (Figure 21).
2. Assuming normality, the distribution parameters of these 24-hour drifts were calculated.
3. The mean (expressed as a percent error) and 95% confidence interval generated from this distribution were used as measures of maximum inaccuracies and precisions of the probes during fieldwork (Table 4).

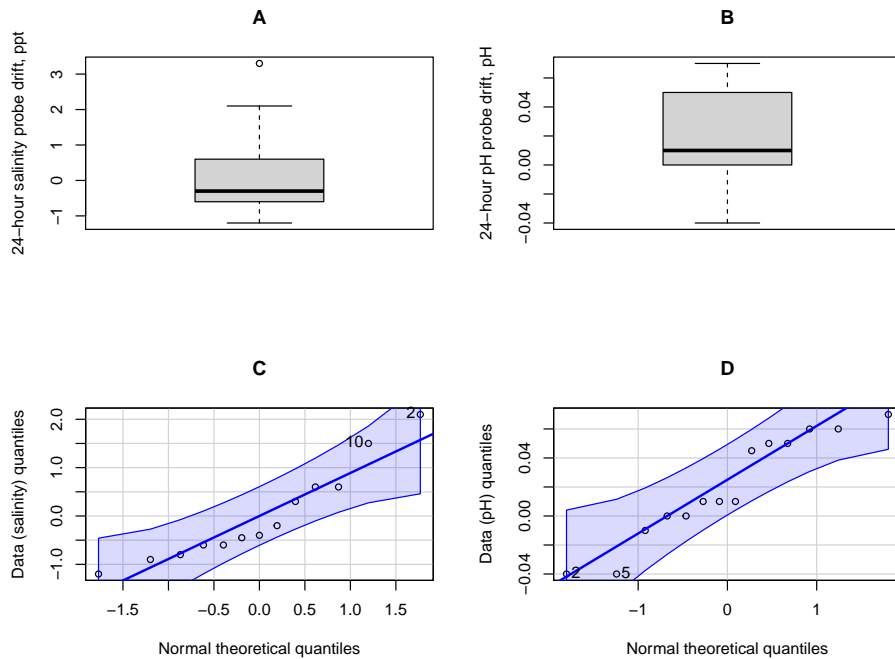


Figure 21: A: Box plot of 24-hour salinity probe drift. Note 3.3 ppt outlier B: Box plot of 24-hour pH probe drift C: Q-Q plots of data quantiles (salinity drift) against theoretical quantiles (outlier excluded;  $W = 0.90$ ,  $p\text{-value} = 0.15$ , respectively) D: Q-Q plots of data quantiles (pH drift) against theoretical quantiles ( $W = 0.92$ ,  $p\text{-value} = 0.19$ ). The 95 % confidence intervals of normality are shown in blue. Each point represents a drift in measurement of standard solution between 0 and 24 hours after calibration.

The 95 % confidence intervals are used in the figures throughout this report. From Table 5, the percent errors and confidence intervals are small enough to confirm that the probes were precise enough to identify significant trends in salinity and pH.

Probe type	Unit	$\bar{x}$	$\hat{\sigma}_m$	Accuracy		Precision 95 % C.I. ( $\pm$ unit)
				Percent error (%)	95 % C.I. ( $\pm$ unit)	
Salinity	ppt	$-3.8 \times 10^{-3}$	0.27	-0.011	0.5	
pH	pH units	0.020	$9.8 \times 10^{-3}$	0.23	0.02	

Table 4: Normal distribution parameters and accuracy/precision measures for 24-hour drift distributions of salinity and pH probes ( $n = 13$  and 14, respectively).  $\bar{x}$ ,  $\hat{\sigma}_m$  and percent error have been given to two decimal places. However, the 95 % confidence intervals have been rounded to the resolution of the respective probes.

## B.2 Titration uncertainty

Repeat titrations were performed on sample EVI-3009. Its alkalinity was assumed to remain constant over time.

During fieldwork, the initial volume ( $V_0$ ) of 0.05N HCl acid used during titrations was reduced from 25 ml to 12.5 ml. A lack of HCl meant just two repeat titrations using  $V_0 = 12.5$  ml were completed. Therefore, I performed another set of repeat titrations on a bottled water sample (sample BUX-2211) in Cambridge. Both sets of titrations are shown in Table 5.

Location	Sample	$V_0$ (ml)	No. of measurements	$\bar{x}$ ( $\mu\text{mol l}^{-1}$ )	95 % C.I. ( $\pm \mu\text{mol l}^{-1}$ )
Field lab	EVI-3009	25	6	4705	68
Field lab	EVI-3009	12.5	2	4655	283
Cambridge	BUX-2211	12.5	5	3453	16

Table 5: Titration precision estimates from repeat titrations of samples EVI-3009 and BUX-2211.

The accuracy of alkalinity measurements was not calculated because the true碱alinitiies of both bottled water samples were unknown.

The  $V_0 = 12.5 \mu\text{mol l}^{-1}$  titrations performed in the field were less precise than those with  $V_0 = 25 \mu\text{mol l}^{-1}$  in lab conditions. Determining the field  $V_0 = 12.5 \mu\text{mol l}^{-1}$  precision was therefore difficult. The 95 % confidence interval of  $\pm 283 \mu\text{mol l}^{-1}$  calculated in the field is used in the results figures. However, the true field precision likely varied, as evidenced by multiple titrations of single samples often varying considerably in their alkalinitiies. Individual precisions are shown as 95 % confidence intervals in figures for repeatedly titrated field samples. Some samples were titrated over 24 hours after collection and produced clearly inaccurate alkalinity measurements, likely due to  $\text{pCO}_2$  equilibration with the atmosphere. These data have been removed from the results.

## B.3 Si uncertainty

$[\text{SiO}_2]$  as measured by spectrophotometry was converted to  $[\text{Si}]$  (both in  $\text{mg l}^{-1}$ ) using

$$[\text{Si}] = [\text{SiO}_2] \times \frac{M_r(\text{Si})}{M_r(\text{SiO}_2)}$$

which was then expressed in  $\mu\text{mol l}^{-1}$ .

Table 6 shows the results of repeated  $[\text{Si}]$  measurements of a sample of Cambridge tap water ( $S_{\text{cam}}$ ), with true  $[\text{Si}] = 138.8 \mu\text{mol l}^{-1}$  by ICP-OES analysis.

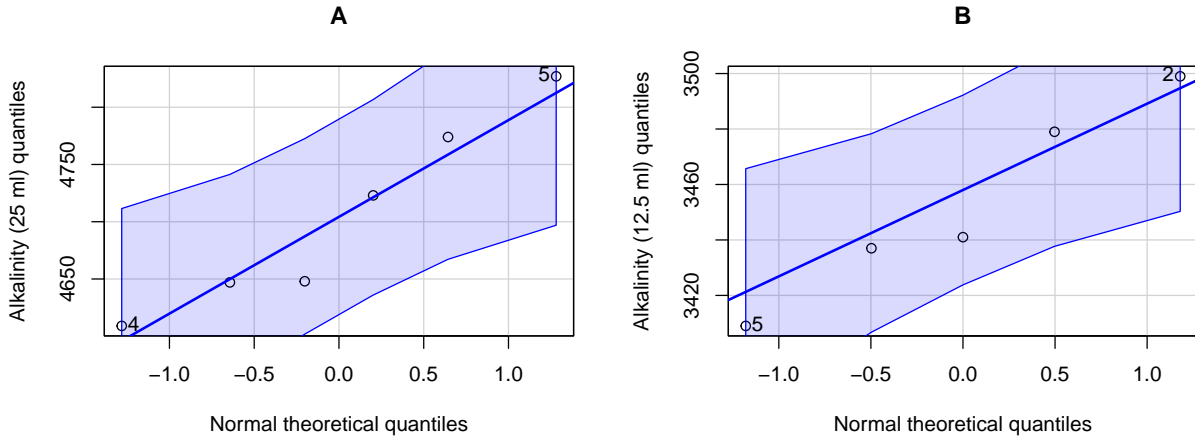


Figure 22: Q-Q plots of data quantiles (alkalinites) against theoretical quantiles for A: titrations performed with  $V_0 = 25 \text{ ml}$  performed in the field and B: titrations performed with  $V_0 = 25 \text{ ml}$  in Cambridge. All points lie within the 95% confidence intervals of normality (A:  $W = 0.93$ , p-value = 0.58 B:  $W = 0.95$ , p-value = 0.77).

$\bar{x} (\mu\text{mol l}^{-1})$	$\hat{\sigma}_m (\mu\text{mol l}^{-1})$	Accuracy Percent error (%)	Precision 95 % C.I. ( $\pm \mu\text{mol l}^{-1}$ )
148.5	13.4	7.0	26

Table 6: Accuracy and precision estimate of [Si] spectrophotometer test using repeat [Si] measurements ( $n = 6$ , excluding a  $575 \mu\text{mol l}^{-1}$  outlier).

All repeated measurements (excluding a  $575 \mu\text{mol l}^{-1}$  outlier) were used to estimate the uncertainty of the  $\text{SiO}_2$  test. The accuracy and precision of the  $\text{SiO}_2$  test likely improved throughout the project as more thorough cuvette cleaning methods were implemented. Anomalously high [Si] recordings were likely due to contamination.

#### B.4 $\text{PO}_4^{3-}$ uncertainty

Repeat  $[\text{PO}_4^{3-}]$  measurements of x9-diluted  $S_{\text{cam}}$  were used to estimate spectrophotometer precision (Table 7). A standard curve from a serial dilution of  $S_{\text{cam}}$  (Figure 23) was used an accepted  $[\text{PO}_4^{3-}]_{\text{cam}}$  to calculate the accuracy of the spectrophotometer.

$\bar{x} (\mu\text{mol l}^{-1})$	$\hat{\sigma}_m (\mu\text{mol l}^{-1})$	Accuracy Percent error (%)	Precision 95 % C.I. ( $\pm \mu\text{mol l}^{-1}$ )
5.2	0.8	55.5	1.5

Table 7: Repeat  $[\text{PO}_4^{3-}]$  measurements ( $n = 4$ ) of x9-diluted  $S_{\text{cam}}$ . Note that this precision interval is significantly larger than the  $\pm 0.2 \mu\text{mol l}^{-1}$  interval on a  $21.1 \mu\text{mol l}^{-1}$  standard given in Hach method 8048.

The accuracy of the spectrophotometer is poor due to the low reference value ( $3.3 \mu\text{mol l}^{-1}$ ). Furthermore, the precision of  $\pm 1.5 \mu\text{mol l}^{-1}$  means observed  $[\text{PO}_4^{3-}]$  deviations smaller than  $\sim 3 \mu\text{mol l}^{-1}$  were not significant.

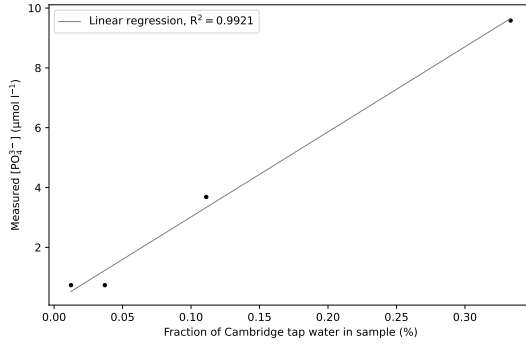


Figure 23:  $[\text{PO}_4^{3-}]$  measurements of serial dilution of  $S_{\text{cam}}$ .

## B.5 $\text{NO}_3^-$ -N to $\text{NO}_3^-$ and uncertainty

$[\text{NO}_3^-]$ -N as measured by spectrophotometry was converted to  $[\text{NO}_3^-]$  (both in  $\text{mg l}^{-1}$ ) using

$$[\text{NO}_3^-] = [\text{NO}_3^- \text{-N}] \times \frac{M_r(\text{NO}_3^-)}{M_r(\text{N})}$$

which was then expressed in  $\mu\text{mol l}^{-1}$ .

$[\text{NO}_3^-]$  measurements were performed on a serial dilution of  $S_{\text{cam}}$  (Figure 24).

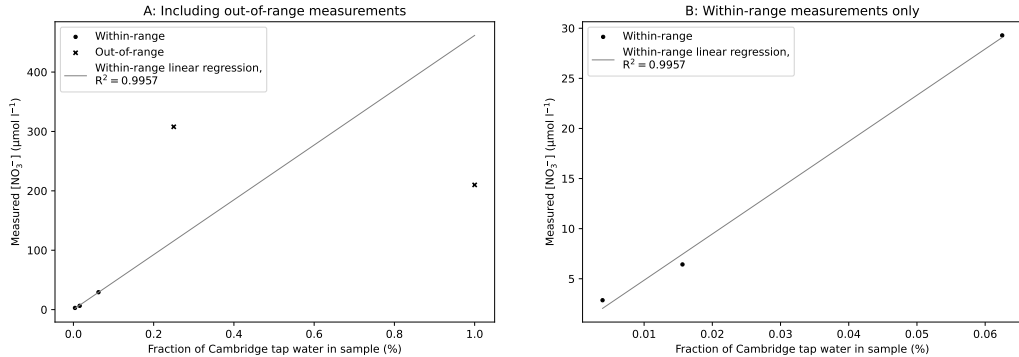


Figure 24:  $[\text{NO}_3^-]$  measurements of serial dilution of  $S_{\text{cam}}$ . A: All measurements, including over-range values (crosses) B: Within-range measurements only.

The standard curve generated from the within-range values (1 to  $36 \mu\text{mol l}^{-1}$  where recorded  $[\text{NO}_3^- \text{-N}]$  in  $\text{mg l}^{-1}$  has been converted to  $[\text{NO}_3^-]$  in  $\mu\text{mol l}^{-1}$ ) is of high quality ( $R^2 = 0.9957$ ), confirming that the  $\text{NO}_3^-$  spectrophotometer test is accurate and precise within its detection range. Extrapolation of the standard curve gives  $[\text{NO}_3^-]_{\text{cam}} = 462 \mu\text{mol l}^{-1}$ . IC analysis gives true  $[\text{NO}_3^-]_{\text{cam}} = 506.3 \mu\text{mol l}^{-1}$ . This  $-8.7\%$  error is likely due to the large extrapolation; however, because the standard curve is of high quality within the detection range, extrapolation may be used to estimate  $[\text{NO}_3^-]$  slightly over the detection limit.

Repeat measurements of  $S_{\text{cam}}$  at a single dilution were not made. The test method sheet (Hach method 8192) gives a precision (95 % confidence interval) of  $\pm 4 \mu\text{mol l}^{-1}$  on a  $29 \mu\text{mol l}^{-1}$   $[\text{NO}_3^-]$  standard. This

precision has been used in figures throughout this report.

## B.6 NH<sub>3</sub>-N as a proxy for NH<sub>4</sub><sup>+</sup> and NH<sub>3</sub>-N uncertainty

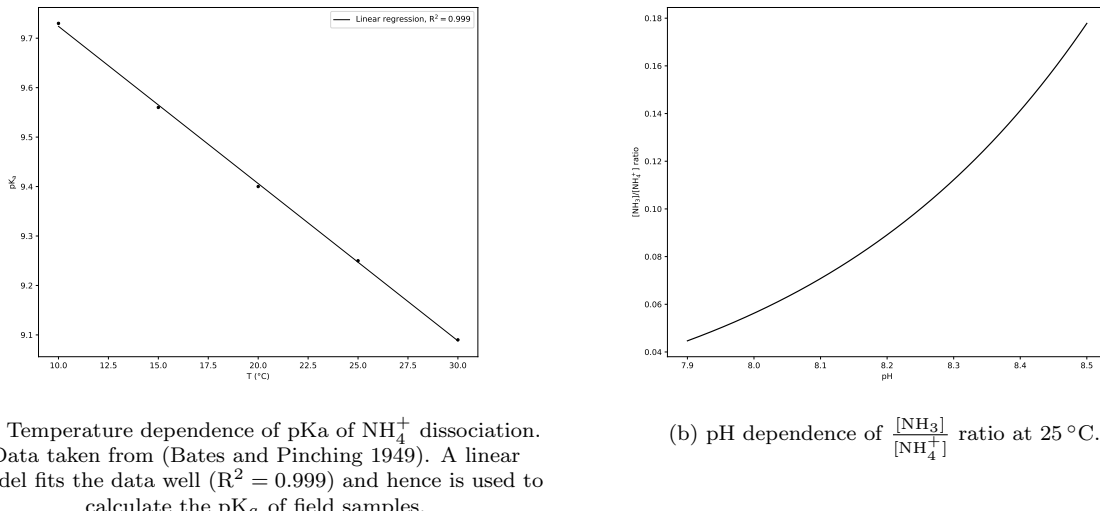
In water, NH<sub>4</sub><sup>+</sup> dissociates according to the reaction



Using the Henderson–Hasselbalch equation, we have

$$\text{pH} = \text{pK}_a + \log_{10} \frac{[\text{NH}_3]}{[\text{NH}_4^+]}$$

The pK<sub>a</sub> of this dissociation reaction is temperature dependent (Figure 25A). Figure 25B shows the  $\frac{[\text{NH}_3]}{[\text{NH}_4^+]}$  dependence on pH at 25 °C.



(a) Temperature dependence of pKa of NH<sub>4</sub><sup>+</sup> dissociation.  
Data taken from (Bates and Pinching 1949). A linear model fits the data well ( $R^2 = 0.999$ ) and hence is used to calculate the pK<sub>a</sub> of field samples.

(b) pH dependence of  $\frac{[\text{NH}_3]}{[\text{NH}_4^+]}$  ratio at 25 °C.

Figure 25

During fieldwork, [NH<sub>3</sub>-N] was measured by spectrophotometry in mg l<sup>-1</sup>. NH<sub>3</sub>-N is the total equilibrium ammonia in the sample ( $[\text{NH}_3] + [\text{NH}_4^+]$ ). Using the sample temperature and pH (recorded during sampling), the above linear model of pKa temperature dependence and Henderson-Hasselbalch equation were used to calculate the [NH<sub>4</sub><sup>+</sup>] of samples in μmol l<sup>-1</sup>.

Repeat [NH<sub>3</sub>-N] measurements of S<sub>cam</sub> were used to estimate spectrophotometer precision (Table 8). The pH and temperature of S<sub>cam</sub> were not measured, so the  $\frac{[\text{NH}_3]}{[\text{NH}_4^+]}$  ratio of the sample was not determined. The uncertainty data are given in mg l<sup>-1</sup>, as recorded. To give a sense of how the NH<sub>3</sub>-N uncertainty data correspond to field NH<sub>4</sub><sup>+</sup> data, these NH<sub>3</sub>-N uncertainty data were converted into [NH<sub>4</sub><sup>+</sup>] in μmol l<sup>-1</sup>, assuming S<sub>cam</sub> was at 25 °C and pH 8.00, to get  $\bar{x} = 1357 \mu\text{mol l}^{-1}$  and 95 % C.I. =  $\pm 45 \mu\text{mol mol}^{-1}$  ( $\pm 3.3 \%$ ).

$\bar{x}$ (mg l <sup>-1</sup> NH <sub>3</sub> -N)	$\hat{\sigma}_m$ (mg l <sup>-1</sup> NH <sub>3</sub> -N)	Precision 95 % C.I. ( $\pm$ mg l <sup>-1</sup> NH <sub>3</sub> -N)
1.37	0.02	0.05

Table 8: Repeat [NH<sub>3</sub>-N] measurements ( $n = 3$ ) of x9-diluted S<sub>cam</sub>. Note that this precision interval is significantly larger than the  $\pm 0.7 \mu\text{mol l}^{-1}$  interval on a  $71.4 \mu\text{mol l}^{-1}$  standard given in Hach method 8038.

[NH<sub>4</sub><sup>+</sup>]<sub>cam</sub> was not determined by independent analysis; therefore, the accuracy of the spectrophotometer cannot be determined. This test's sensitivity is reduced by up to 30 % by the high [Cl<sup>-</sup>] found in seawater.

## C Data table

Sample ID	[Ba <sup>2+</sup> ] (mg l <sup>-1</sup> )	[Ca <sup>2+</sup> ] (mg l <sup>-1</sup> )	[K <sup>+</sup> ] (mg l <sup>-1</sup> )	[Li <sup>+</sup> ] (mg l <sup>-1</sup> )	[Mg <sup>2+</sup> ] (mg l <sup>-1</sup> )	[Na <sup>+</sup> ] (mg l <sup>-1</sup> )	[S] (mg l <sup>-1</sup> )	[Si] (mg l <sup>-1</sup> )	[Sr <sup>2+</sup> ] (mg l <sup>-1</sup> )	[NO <sub>3</sub> <sup>-</sup> ] (μmol l <sup>-1</sup> )	[Cl <sup>-</sup> ] (μmol l <sup>-1</sup> )	[SO <sub>4</sub> <sup>2-</sup> ] (μmol l <sup>-1</sup> )
CDL-2509-03	0.01	814.38	974.54	0.26	2020.47	20083.35	1888.19	1.15	13.83	605526.1	31733.64	
CDL-2509-05	0.01	442.24	486.31	0.14	1262.84	11183.27	1030.21	0.81	7.57	3.62496	603368.5	31667.77
LVI-1909-05	0.00285	113.2052	2.48224	0.003238	16.23706	39.80764	16.1967	6.35375	0.198353	29.92458	1421.662	439.6895
LVI-2109-07	0.00238	116.4482	2.85581	0.003561	20.58328	73.41011	15.92918	6.39309	0.22126	11.8039	2958.233	441.7679
LVI-2509-01	0.01	301.39	267.99	0.08	782.61	6613.34	609.39	1.88	4.46		351347.6	18229.6
LVI-2509-02	0.01	334	313.99	0.09	886	7648.91	702.85	1.63	5.1		400913.3	20891.22
LVI-2509-03	0.00179	311.5372	264.124	0.107351	803.3502	6667.604	566.1827	3.4616	4.87477		298633.5	15369.65
LVI-2509-04	0.01	232.73	167.78	0.05	516.45	4307.29	395.64	2.58	2.92		217969.8	11422.21
LVI-2509-05	0.00197	213.5915	93.6398	0.045566	398.0595	3267.178	280.8824	5.56935	2.46523		142193	7446.764
VIS-2609-01	0.00177	516.2225	506.0987	0.225938	1618.626	13435.73	1138.109	1.39996	9.782947		602566.7955	31550.79144
BOU-2809-01	0.00165	520.02179	512.3756	0.227267	1634.899315	13527.78326	1147.17232	1.78993	9.844813333		616601.0144	32260.5084
BOU-2809-04	0.00126	510.01898	514.00494	0.22594	1629.857705	13495.48517	1141.48843	1.17752	9.77994			
BOU-2809-05	0.00126	510.01898	514.00494	0.22594	1629.857705	13495.48517	1141.48843	1.17752	9.77994		608719.5584	31839.53832
CDL-2909-01	0.00138	513.41602	515.32293	0.225281	1629.408293	13439.0491	1142.5164	0.37729	9.77557		583924.3	30361.02
CDL-2909-02	0.00132	515.31016	516.15675	0.224558	1624.575985	13379.84424	1144.6693	0.12504	9.760593333	2.57406	611554.5594	32058.6
CDL-2909-03	0.00132	515.31016	516.15675	0.224558	1624.575985	13379.84424	1144.6693	0.12504	9.760593333			
MED-2609-01	0.00047	480.46555	464.40012	0.211528	1517.457253	12506.9596	1068.5151	-0.3343	9.1543		569054.1709	29790.19784
LVI-2909-05	0.00174	527.56405	516.28062	0.229756	1664.142398	13707.24813	1179.63449	0.76234	9.975063333		605824.1542	31587.12304
NVR-2709-01	0.04	142.55	20.07	0.01	80.85	493.64	59.45	5.16	0.64		12981.712	751.50484

Table 9: Raw ICP-OES and IC data.

Sample ID	Location	Date	Time	T (°C)	pH	TDS (mg l <sup>-1</sup> )	Cond. (µSv)	Alkalinity (µmol l <sup>-1</sup> )	Salinity (ppt)	[NO <sub>3</sub> <sup>-</sup> -N] (mg l <sup>-1</sup> )	[PO <sub>4</sub> <sup>3-</sup> ] (mg l <sup>-1</sup> )	[NH <sub>3</sub> <sup>-</sup> -N] (mg l <sup>-1</sup> )	[SiO <sub>2</sub> ] (mg l <sup>-1</sup> )	Longitude	Latitude	Titration delay (d)	V <sub>0</sub> (ml)		
BOU-1509-01	Bouzigues	15/09/2023	14:05:00	23.9	8.00	2000	4000	1959	40.2	0.01	0.43				3.651143	43.447557	0	25	
BOU-1509-02	Bouzigues	15/09/2023	14:06:00	25.4	8.01	2000	4000	1980	40.0						3.651043	43.447452	0	25	
BOU-1509-03	Bouzigues	15/09/2023	14:17:00	24.8	8.01	2000	4000	1991	40.1	0.01					3.652147	43.447741	N/A	25	
BOU-1509-04	Bouzigues	15/09/2023	14:09:00	24.8	8.05	2000	4000	1971	40.1	0.01	0.78				3.653957	43.446818	N/A	25	
BOU-1509-05	Bouzigues	15/09/2023	14:09:00	24.8	8.04	2000	4000	2012	40.1	0.01					3.653957	43.446818	N/A	25	
BOU-1509-06	Bouzigues	15/09/2023	14:15:00												3.652205	43.448141			
BOU-1509-07	Bouzigues	15/09/2023	14:24:00												3.652996	43.448162			
CDL-1909-01	Angle cove	19/09/2023	12:49:00	25.6	8.13	2000	4000		41.2						3.667494	43.452282			
CDL-1909-02	Angle cove	19/09/2023	12:56:00	24.9					40.6		1.26				3.669288	43.452470			
CDL-1909-03	Angle cove	19/09/2023	13:00:00	24.6					40.6						3.670594	43.452738			
CDL-1909-04	Angle cove	19/09/2023	13:05:00	24.7	8.06	2000	4000	2149	40.8	0.01	12.06				3.672186	43.451940	0	25	
CDL-1909-05	Angle cove	19/09/2023	13:33:00												3.675303	43.452085			
CDL-1909-06-01	Angle cove	19/09/2023	13:34:00	25.2					41.1		1.98				3.676822	43.451743			
CDL-1909-06-02	Angle cove	19/09/2023	13:34:00	25.2					41.1		0.04				3.676822	43.451743			
CDL-1909-06-03	Angle cove	19/09/2023	13:34:00	25.2					41.1		0.07				3.678386	43.451013			
CDL-1909-07	Angle cove	19/09/2023	13:39:00	25.8					41.2						3.668476	43.455083			
CDL-1909-08	Angle cove	19/09/2023	14:25:00	25.4					40.6						3.671141	43.457043	1	25	
CDL-1909-09	Angle cove	19/09/2023	14:37:00	24.7	8.10	2000	4000	2499	41.2	0.01	0.26				3.672034	43.460118			
CDL-1909-10-01	Angle cove	19/09/2023	14:40:00	25.9	8.20	2000	4000	3278	40.6	0.06	0.06				3.671408	43.458476	1	25	
CDL-1909-10-02	Angle cove	19/09/2023	14:40:00	25.9	8.20	2000	4000	2670	40.6	0.06	0.06				3.671408	43.458476	1	25	
CDL-1909-11	Angle cove	19/09/2023	15:02:00												3.674411	43.462799			
CDL-2509-01-01	Angle cove	25/09/2023	17:19:00						40.0		0.05				3.672034	43.460118			
CDL-2509-01-02	Angle cove	25/09/2023	17:19:00						40.0		0.05				3.672034	43.460118			
CDL-2509-01-03	Angle cove	25/09/2023	17:19:00						40.0						3.672034	43.460118			
CDL-2509-02	Angle cove	25/09/2023	17:22:00						40.1						3.673394	43.458683			
CDL-2509-03	Angle cove	25/09/2023	17:25:00						39.5						3.675707	43.457566			
CDL-2509-04-01	Angle cove	25/09/2023	17:27:00						40.0		0.04				3.677005	43.456307			
CDL-2509-04-02	Angle cove	25/09/2023	17:27:00						40.0		0.03				3.677005	43.456307			
CDL-2509-04-03	Angle cove	25/09/2023	17:27:00						40.0		0.05				3.678304	43.455197			
CDL-2509-05	Angle cove	25/09/2023	17:29:00						39.8						3.677128	43.464751	N/A	25	
LVI-1409-01	Vène river	14/09/2023	13:03:00	26.5	7.99	2000	4000	2284	40.7						3.672028	43.460509	0	25	
LVI-1409-02	Vène river	14/09/2023	13:09:00	28.0	8.33	2000	4000	2711	42.5						3.672088	43.460444	0	25	
LVI-1409-03	Vène river	14/09/2023	13:45:00	26.1	7.98	2000	4000	2203	41.5						3.672478	43.459910	0	25	
LVI-1409-04	Vène river	14/09/2023	14:26:00	25.6	7.93	2000	4000	2143	45.0	0.01	0.99				3.676053	43.458648	0	25	
LVI-1509-01	Vène river	15/09/2023	15:14:00	23.3	7.91	442	883	4358	0.7	0.03					3.685754	43.467752	N/A	25	
LVI-1709-01	Vène river	17/09/2023	15:06:00	24.6	7.61	2000	4000	2452	17.0						3.680603	43.464751	2	25	
LVI-1709-02	Vène river	17/09/2023	15:21:00	25.0	7.75	2000	4000	2420	20.4						3.680157	43.464724	2	25	
LVI-1709-03	Vène river	17/09/2023	16:50:00	25.7	7.95	2000	4000	2396	22.7						3.674321	43.463101	0	25	
LVI-1909-01	Vène river	19/09/2023	15:12:00	25.3	8.03	2000	4000	3338	16.2		0.25				3.675125	43.464168	N/A	25	
LVI-1909-02	Vène river	19/09/2023	15:21:00	24.9				3305	12.3	0.01	0.53				3.677718	43.464828	1	25	
LVI-1909-03-01	Vène river	19/09/2023	15:33:00	24.0	7.64	2000	4000	3475	6.1		0.12	0.24			3.680553	43.464737	1	25	
LVI-1909-04	Vène river	19/09/2023	15:53:00	24.5	7.70	2000	4000	3330	12.1		0.21				3.680121	43.464657	1	25	
LVI-1909-05	Vène river	19/09/2023	16:38:00	8.03	503	1015	4193	0.6	0.05	0.19					3.685724	43.467717	0	25	
LVI-2109-01	Vène river	21/09/2023	10:56:00	23.0	7.88			3414	18.4						3.680602	43.464727			
LVI-2109-02	Vène river	21/09/2023	11:19:00	23.0	8.10			3662	14.1		0.21				3.680283	43.464608			
LVI-2109-03-01	Vène river	21/09/2023	18:42:00	21.6	8.07			3906	3.3			0.37			3.680423	43.464645			
LVI-2109-03-02	Vène river	21/09/2023	18:42:00					5892	3.3						3.680423	43.464645	3	12.5	
LVI-2109-03-03	Vène river	21/09/2023	18:42:00					4278	3.3						3.680423	43.464645	3	12.5	
LVI-2109-06	Vène river	21/09/2023	18:43:00	23.1	7.89	2000	4000	2341	41.2		0.18				3.671927	43.460493	N/A	25	
LVI-2109-07	Vène river	21/09/2023	14:39:00	21.9	8.43	608	1228	4769	0.5		0.13				3.685855	43.467733	N/A	25	
LVI-2309-01	Vène river	23/09/2023	10:52:00	20.0					40.4						3.671849	43.460389			
LVI-2309-02-01	Vène river	23/09/2023	11:50:00	19.5				3349	34.4						4.7	3.670900	43.459664	1	25
LVI-2309-03	Vène river	23/09/2023	12:17:00	20.4	7.96			2270	42.6						3.671311	43.459239	0	25	
LVI-2309-04	Vène river	23/09/2023	12:27:00	19.8	6.65			3309	25.0						3.673912	43.462346	0	25	
LVI-2309-05-01	Vène river	23/09/2023	13:43:00	19.2	7.03			4368	6.3						3.679705	43.464731	N/A	25	
LVI-2309-05-02	Vène river	23/09/2023	13:43:00	19.2	7.03			4368	6.3						3.679705	43.464731	N/A	25	
LVI-2309-05-03	Vène river	23/09/2023	13:43:00	19.2	7.03			4368	6.3		0.28				7.6	3.679705	43.464731	N/A	25
LVI-2309-06-01	Vène river	23/09/2023	14:09:00	20.1				4153	7.7						3.679125	43.464830	1	25	
LVI-2309-07-01	Vène river	23/09/2023	14:29:00	19.0	8.41			4570	0.4	0.14	0.26				9.4	3.685832	43.467765	0	25
LVI-2509-01-01	Vène river	25/09/2023	N/A	8.16	2000	4000	3047	25.6							1.7	3.674363	43.463516	0	12.5
LVI-2509-02-01	Vène river	25/09/2023	18:00:00	8.15	2000	4000	3218	28.6		0.10					5.2	3.674772	43.463811	0	12.5
LVI-2509-03-01	Vène river	25/09/2023	N/A	8.28	2000	4000	3480	22.2							5.5	3.674384	43.463687	0	12.5
LVI-2509-03-02	Vène river	25/09/2023	N/A					3546	22.2						10.3	3.674384	43.463687	0	12.5
LVI-2509-03-03	Vène river	25/09/2023	N/A					3698	22.2						17.0	3.674384	43.463687	0	12.5
LVI-2509-03-04	Vène river	25/09/2023	N/A					3698	22.2						4.9	3.674384	43.463687	0	12.5
LVI-2509-04-01	Vène river	25/09/2023	N/A		8.17			3952	14.8						5.0	3.675286	43.464127	0	12.5
LVI-2509-04-02	Vène river	25/09/2023	N/A					4197											

Sample ID	Location	Date	Time	T (°C)	pH	TDS (mg l <sup>-1</sup> )	Cond. (µSv)	Alkalinity (µmol l <sup>-1</sup> )	Salinity (ppt)	[NO <sub>3</sub> <sup>-</sup> -N] (mg l <sup>-1</sup> )	[PO <sub>4</sub> <sup>3-</sup> ] (mg l <sup>-1</sup> )	[NH <sub>3</sub> <sup>-</sup> -N] (mg l <sup>-1</sup> )	[SiO <sub>2</sub> ] (mg l <sup>-1</sup> )	Longitude	Latitude	Titration delay (d)	V <sub>0</sub> (ml)		
SM-1409-11	NE Thau	14/09/2023	14:13:00	28.4					39.9						3.671956	43.46015			
SM-1409-12	NE Thau	14/09/2023	14:16:00	27.4					40.4						3.672734	43.45924			
SM-1409-13	NE Thau	14/09/2023	14:19:00	26.2					40.8						3.673465	43.45851			
SM-1409-14	NE Thau	14/09/2023	14:22:00	25.8					41.4						3.674323	43.45838			
SM-1509-01	NE Thau	15/09/2023	14:12:00	25.0					40.0						3.653632	43.44702			
SM-1509-02	NE Thau	15/09/2023	14:13:00	24.8					40.2						3.653018	43.44746			
SM-1509-03	NE Thau	15/09/2023	14:14:00	24.9					40						3.652619	43.44763			
SM-1609-01	NE Thau	16/09/2023	10:07:00	24.5					42.5						3.67198	43.44351			
SM-1609-02	NE Thau	16/09/2023	10:08:00	24.6					42.6						3.671755	43.44374			
SM-1609-03	NE Thau	16/09/2023	10:10:00	24.7					42.7						3.671629	43.44433			
SM-1609-04	NE Thau	16/09/2023	10:05:00	24.7					42.6						3.672346	43.44355			
SM-1609-05	NE Thau	16/09/2023	10:04:00	24.6					42.6						3.673045	43.44361			
SM-1609-06	NE Thau	16/09/2023	11:45:00	24.9					42.2						3.671917	43.44366			
SM-1609-07	NE Thau	16/09/2023	11:32:00	24.7					42.4						3.671417	43.44335			
SM-1609-08	NE Thau	16/09/2023	11:32:00	24.6					42.6						3.67047	43.44307			
SM-1909-01	NE Thau	19/09/2023	14:45:00	25.4					38.6						3.670977	43.45994			
SM-1909-02	NE Thau	19/09/2023	14:47:00	25.7					34.7						3.671757	43.46036			
SM-1909-02	NE Thau	19/09/2023	18:39:00	25.7					34.7						3.670977	43.45994			
SM-1909-03	NE Thau	19/09/2023	14:50:00	26.6					36.6						3.672842	43.46149			
SM-1909-03	NE Thau	19/09/2023	18:38:00	26.6					36.6						3.672842	43.46149			
SM-1909-04	NE Thau	19/09/2023	14:52:00	25.8					31.6						3.673478	43.46224			
SM-1909-04	NE Thau	19/09/2023	18:38:00	25.8					31.6						3.673478	43.46224			
SM-1909-05	NE Thau	19/09/2023	14:56:00	26.1					29.1						3.67438	43.46275			
SM-1909-05	NE Thau	19/09/2023	18:37:00	26.1					29.1						3.67438	43.46275			
SM-1909-06	NE Thau	19/09/2023	15:07:00	27.0					28.9						3.67433	43.46328			
SM-1909-07	NE Thau	19/09/2023	15:09:00	26.8					28.6						3.674504	43.46378			
SM-1909-08	NE Thau	19/09/2023	15:16:00	24.5					15.4						3.676246	43.46423			
SM-2109-01	NE Thau	21/09/2023	12:36:00	24.3					24.3						3.67429	43.46313			
SM-2109-02	NE Thau	21/09/2023	18:43:00	24.8					28.2						3.674073	43.46234			
SM-2309-01	NE Thau	23/09/2023	09:42:00	17.1					17.7						3.674416	43.46315			
SM-2309-02	NE Thau	23/09/2023	09:45:00	17.5					19.5						3.674479	43.46303			
SM-2309-03	NE Thau	23/09/2023	09:49:00	16.3					18.3						3.674417	43.46274			
SM-2309-04	NE Thau	23/09/2023	09:52:00	18.4					23.7						3.673977	43.46235			
SM-2309-05	NE Thau	23/09/2023	10:02:00	16.6					20.8						3.673558	43.46224			
SM-2309-06	NE Thau	23/09/2023	10:06:00	17.2					23.3						3.673367	43.46213			
SM-2309-07	NE Thau	23/09/2023	10:09:00	25.0					17.5						3.673083	43.46192			
SM-2309-08	NE Thau	23/09/2023	10:16:00	16.8					22.1						3.673004	43.46185			
SM-2309-09	NE Thau	23/09/2023	10:23:00	17.8					25.4						3.672783	43.46137			
SM-2309-10	NE Thau	23/09/2023	10:21:00	18.9					42.6						3.672276	43.46106			
SM-2309-11	NE Thau	23/09/2023	10:29:00	19.2					29.1						3.671276	43.46064			
SM-2309-12	NE Thau	23/09/2023	10:32:00	17.8					25.6						3.671869	43.4604			
SM-2309-13	NE Thau	23/09/2023	10:41:00	18.4					28.6						3.671803	43.46046			
SM-2309-14	NE Thau	23/09/2023	11:08:00	20.0					40.6						3.671794	43.46042			
SM-2309-15	NE Thau	23/09/2023	11:13:00	18.4					29.9						3.670932	43.45971			
SM-2309-16	NE Thau	23/09/2023	11:23:00						36.7						3.671312	43.45924			
SM-2309-17	NE Thau	23/09/2023	11:17:00	20.0											3.671259	43.4594			
SM-2309-18	NE Thau	23/09/2023	12:20:00	20.7					20.8						3.674424	43.46301			
SM-2309-19	NE Thau	23/09/2023	13:17:00	20.2					1.9						3.681702	43.46541			
SM-2309-20	NE Thau	23/09/2023	13:26:00	19.6					3.8						3.680583	43.46466			
SM-2309-21	NE Thau	23/09/2023	13:59:00						7.3						3.679154	43.46477			
SM-2309-22	NE Thau	23/09/2023	13:55:00						7.2						3.679041	43.46481			
SM-2309-23	NE Thau	23/09/2023	00:00:00						7.3						3.679153	43.46477			
VIS-1609-01	Vise spring	16/09/2023	09:27:00	24.2	7.93	2000	4000	2303	40.4						3.67364	43.44367	0	25	
VIS-1609-02	Vise spring	16/09/2023	10:18:00	8.00	2000	4000	2040	42.6							3.671914	43.44364	0	25	
VIS-1609-03	Vise spring	16/09/2023	11:04:00	24.9	7.90	2000	4000	1565	42.2						3.671917	43.44366	0	25	
VIS-1809-01	Vise spring	18/09/2023	14:27:00	28.4	8.11	2000	4000		39.7			0.07			3.6737	43.44372			
VIS-2609-01	Vise spring	26/09/2023	15:05:00	24.3					39.8						3.673083	43.44086			
VIS-2609-02	Vise spring	26/09/2023	15:04:00	23.0					39.8						3.671678	43.43854			
SM-2309-24	NE Thau	23/09/2023	13:36:00						3.8						3.680116	43.46457			
BOU-2809-01	Bouzigue	28/09/2023	11:00:00	23.0	8.02	2000	4000	2104	39.8			-0.01			3.652063	43.44806	0	25	
BOU-2809-02	Bouzigue	28/09/2023	11:42:00	24.4					39.9						3.652307	43.44714			
BOU-2809-03	Bouzigue	28/09/2023	11:42:00	23.3					40.0						3.652753	43.44623			
BOU-2809-04-01	Bouzigue	28/09/2023	11:42:00	22.3	6.89			2109	40.0	0.01	0.06	-0.02	3.5		3.6528	43.44605	0	25	
BOU-2809-05-01	Bouzigue	28/09/2023	11:42:00	23.7	8.02			2078	40.2	0.01	0.05	0.01	4.6		3.652782	43.44602	0	25	
LVI-2809-01-01	Vène river	28/09/2023	16:04:00	25.1	8.14	2000	4000	3326	24.0						5.5	3.674388	43.46318	0	25
LVI-2809-02	Vène river	28/09/2023	16:15:00	25.4	8.21	2000	4000	3746	17.3						3.674316	43.46354	0	25	
LVI-2809-01	Vène river	29/09/2023	09:50:00	18.8	8.37	721	1433	4703	0.5						3.685754	43.46775	0	25	
LVI-2909-02	Vène river	29/09/2023	10:56:00	20.5					11.8						3.675387	43.46408			
LVI-2909-04	Vène river	29/09/2023	11:08:00					2499	41.3						3.671359	43.45917	0	25	
CDL-2909-01-01	Angle cove	29/09/2023	11:20:00												1.7	3.677061	43.45628		
CDL-2909-01-02	Angle cove	29/09/2023	11:20:00												2.1	3.677061	43.45628		
CDL-2909-01-03	Angle cove	29/09/2023	11:20:00												2.3	3.677061	43.45628		
CDL-2909-02-01	Angle cove	29/09/2023	11:24:00												4.5	3.675569	43.4555		
CDL-2909-02-02	Angle cove	29/09/2023	11:24:00												3.675569	43.4555			
CDL-2909-02-03	Angle cove	29/09/2023	11:24:00												3.675569	43.4555			
CDL-2909-03	Angle cove	29/09/2023	11:27:00												3.674116	43.45456			
LVI-2909-03	Vène river	29/09/2023	11:40:00	23.1					30.1						3.67432	43.46315			
NVR-1809-01	Nègue-Vauques	18/09/2023	11:59:00	25.6	7.80	1930	3870	3145	2.3	0.02	0.11	0.16			3.570757	43.4104	0	25	
CDM-1809-01	Canal du Midi	18/09/2023	14:10:00	24.4	7.98				19.1			0.18			3.531996	43.32151			
MED-1809-01	Med. Sea	18/09/2023	08:50:00	23.8	7.98				37.3	0.01	0.05	0.08	3.3		3.700096	43.39551			
MED-2609-01	Med. Sea	26/09/2023	N/A	24.3	8.16	2000	4000	2175	37.5						3.67432	43.46315	0	12.5	
LVI-2909-05																			

## References

- “Garrigue” and “Maquis” — Parc national des calanques (2023). URL: <https://www.calanques-parcnational.fr/en/garrigue-and-maquis> (visited on 11/22/2023).
- Bacher, Cédric, Hélène Bioteau, and Annie Chapelle (Sept. 1995). “Modelling the impact of a cultivated oyster population on the nitrogen dynamics: The Thau Lagoon case (France)”. en. In: *Ophelia* 42.1, pp. 29–54. ISSN: 0078-5326. DOI: 10.1080/00785326.1995.10431496. URL: <http://www.tandfonline.com/doi/abs/10.1080/00785326.1995.10431496> (visited on 10/26/2023).
- Bates, Roger G. and Gladys D. Pinching (May 1949). “Acidic dissociation constant of ammonium ion at 0 to 50 C, and the base strength of ammonia”. en. In: *Journal of Research of the National Bureau of Standards* 42.5, p. 419. ISSN: 0091-0635. DOI: 10.6028/jres.042.037. URL: [https://nvlpubs.nist.gov/nistpubs/jres/42/jresv42n5p419\\_A1b.pdf](https://nvlpubs.nist.gov/nistpubs/jres/42/jresv42n5p419_A1b.pdf) (visited on 01/11/2024).
- De Casabianca, M.-L., T. Laugier, and D. Collart (July 1997). “Impact of shellfish farming eutrophication on benthic macrophyte communities in the Thau lagoon, France”. en. In: *Aquaculture International* 5.4, pp. 301–314. ISSN: 1573-143X. DOI: 10.1023/A:1018308022436. URL: <https://doi.org/10.1023/A:1018308022436> (visited on 01/15/2024).
- Dem'Eaux Thau (2024). *Dem'Eaux Thau: management of groundwater resources in a coastal karst aquifer* — BRGM. en. URL: <https://www.brgm.fr/en/reference-completed-project/dem-eaux-thau-management-groundwater-resources-coastal-karst-aquifer> (visited on 01/12/2024).
- Eutrophication (2024). *Eutrophication: Causes, Consequences, and Controls in Aquatic Ecosystems* — Learn Science at Scitable. en. Cg\_cat: Eutrophication: Causes, Consequences, and Controls in Aquatic Ecosystems Cg\_level: MED Cg\_topic: Eutrophication: Causes, Consequences, and Controls in Aquatic Ecosystems. URL: <https://www.nature.com/scitable/knowledge/library/eutrophication-causes-consequences-and-controls-in-aquatic-102364466/> (visited on 01/15/2024).
- Frenod, Emmanuel (2013). “Modeling confinement in Étang de Thau: Numerical simulations and multi-scale aspects”. en. In: *Conference Publications*. AIMS Press. ISBN: 978-1-60133-016-1. DOI: 10.3934/proc.2013.2013.69. URL: <http://aimsciences.org/article/doi/10.3934/proc.2013.2013.69> (visited on 10/17/2023).
- Gaillardet, J. et al. (July 1999). “Global silicate weathering and CO<sub>2</sub> consumption rates deduced from the chemistry of large rivers”. en. In: *Chemical Geology* 159.1-4, pp. 3–30. ISSN: 00092541. DOI: 10.1016/S0009-2541(99)00031-5. URL: <https://linkinghub.elsevier.com/retrieve/pii/S0009254199000315> (visited on 10/31/2023).
- Gieskes, Joris M. (1998). “Earth’s ocean geochemistry”. en. In: *Geochemistry*. ISSN: 1871-756X. Springer, Dordrecht, pp. 168–179. ISBN: 978-1-4020-4496-0. DOI: 10.1007/1-4020-4496-8\_86. URL: [https://link.springer.com/referenceworkentry/10.1007/1-4020-4496-8\\_86](https://link.springer.com/referenceworkentry/10.1007/1-4020-4496-8_86) (visited on 01/09/2024).
- Jouffre, Didier and Michel Amanieu (Jan. 1991). “Ecothau. Synthèse des résultats”. fr. In: URL: <https://archimer.ifremer.fr/doc/00060/17168/> (visited on 01/08/2024).
- Ladouce, B. et al. (Sept. 2023). “Dataset on onshore groundwaters and offshore submarine spring of a Mediterranean karst aquifer during flow reversal and saltwater intrusion”. In: *Data in Brief* 50, p. 109557. ISSN: 2352-3409. DOI: 10.1016/j.dib.2023.109557. URL: <https://www.ncbi.nlm.nih.gov/pmc/articles/PMC10518333/> (visited on 01/10/2024).
- Lane, Todd W. and François M. M. Morel (Apr. 2000). “A biological function for cadmium in marine diatoms”. In: *Proceedings of the National Academy of Sciences* 97.9. Publisher: Proceedings of the National

- Academy of Sciences, pp. 4627–4631. DOI: 10.1073/pnas.090091397. URL: <https://www.pnas.org/doi/full/10.1073/pnas.090091397> (visited on 11/02/2023).
- Maréchal, Jean Christophe et al. (Mar. 2022). *Flow reversal and saltwater intrusion at the submarine spring of a Mediterranean karst aquifer : explanation and modelling.* en. Tech. rep. IAHS2022-530. Conference Name: IAHS2022. Copernicus Meetings. DOI: 10.5194/iahs2022-530. URL: <https://meetingorganizer.copernicus.org/IAHS2022/IAHS2022-530.html> (visited on 01/12/2024).
- Mesnage, Valérie et al. (Apr. 2007). “Nutrient dynamics at the sediment–water interface in a Mediterranean lagoon (Thau, France): Influence of biodeposition by shellfish farming activities”. In: *Marine Environmental Research* 63.3, pp. 257–277. ISSN: 0141-1136. DOI: 10.1016/j.marenvres.2006.10.001. URL: <https://www.sciencedirect.com/science/article/pii/S0141113606001887> (visited on 11/01/2023).
- Obermann, Matthias, Jochen Froebrich, et al. (Feb. 2007). “Impact of significant floods on the annual load in an agricultural catchment in the mediterranean”. en. In: *Journal of Hydrology* 334.1-2, pp. 99–108. ISSN: 00221694. DOI: 10.1016/j.jhydrol.2006.09.029. URL: <https://linkinghub.elsevier.com/retrieve/pii/S0022169406005154> (visited on 11/01/2023).
- Obermann, Matthias, Karl-Heinz Rosenwinkel, and Marie-George Tournoud (July 2009). “Investigation of first flushes in a medium-sized mediterranean catchment”. In: *Journal of Hydrology* 373.3, pp. 405–415. ISSN: 0022-1694. DOI: 10.1016/j.jhydrol.2009.04.038. URL: <https://www.sciencedirect.com/science/article/pii/S0022169409002947> (visited on 11/01/2023).
- Oysters and mussels* (2023). en-GB. URL: <http://coquithau.com/en/oysters-and-mussels/> (visited on 11/15/2023).
- Pétré, Marie-Amélie et al. (July 2020). *Hydraulic and geochemical impact of occasional saltwater intrusions through a submarine spring in a karst and thermal aquifer (Balaruc peninsula near Montpellier, France).* en. preprint. Groundwater hydrology/Modelling approaches. DOI: 10.5194/hess-2020-292. URL: <https://hess.copernicus.org/preprints/hess-2020-292/hess-2020-292.pdf> (visited on 01/12/2024).
- Picot, Bernadette et al. (1990). “Interpretation of the seasonal variations of nutrients in a mediterranean lagoon: étang de Thau”. en. In: *Hydrobiologica* 207, pp. 105–114.
- Plus, Martin et al. (Mar. 2006). “Modelling water discharges and nitrogen inputs into a Mediterranean lagoon”. en. In: *Ecological Modelling* 193.1-2, pp. 69–89. ISSN: 03043800. DOI: 10.1016/j.ecolmodel.2005.07.037. URL: <https://linkinghub.elsevier.com/retrieve/pii/S0304380005004576> (visited on 10/26/2023).
- Rosenfeld, Jeffrey K. (1979). “Ammonium adsorption in nearshore anoxic sediments1”. en. In: *Limnology and Oceanography* 24.2. \_eprint: <https://onlinelibrary.wiley.com/doi/pdf/10.4319/lo.1979.24.2.0356>, pp. 356–364. ISSN: 1939-5590. DOI: 10.4319/lo.1979.24.2.0356. URL: <https://onlinelibrary.wiley.com/doi/abs/10.4319/lo.1979.24.2.0356> (visited on 01/12/2024).
- Sarmiento, Jorge Louis and Nicolas Gruber (2006). *Ocean biogeochemical dynamics.* en. OCLC: ocm60651167. Princeton: Princeton University Press. ISBN: 978-0-691-01707-5.
- Time Series: Thau Lagoon* (2024). URL: <https://www.st.nmfs.noaa.gov/copepod/time-series/fr-10201/> (visited on 01/09/2024).
- Trombetta, Thomas et al. (Sept. 2021). “Co-occurrence networks reveal the central role of temperature in structuring the plankton community of the Thau Lagoon”. In: *Scientific Reports* 11, p. 17675. ISSN: 2045-2322. DOI: 10.1038/s41598-021-97173-y. URL: <https://www.ncbi.nlm.nih.gov/pmc/articles/PMC8417261/> (visited on 11/01/2023).

Vaulot, D (Jan. 1986). "Phytoplanktonic productivity and nutrients in five Mediterranean lagoons". en. In: *Deep Sea Research Part B. Oceanographic Literature Review* 33.12, p. 1026. ISSN: 01980254. doi: 10.1016/0198-0254(86)94507-3. URL: <https://linkinghub.elsevier.com/retrieve/pii/0198025486945073> (visited on 01/10/2024).